The Astrophysical Journal Supplement Series, 252:23 (19pp), 2021 February https://doi.org/10.3847/1538-4365/abcb81

OGLE-ing the Magellanic System: Optical Reddening Maps of the Large and Small Magellanic Clouds from Red Clump Stars

D. M. Skowron[1], J. Skowron[1], A. Udalski[1], M. K. Szymański[1], I. Soszyński[1], Ł. Wyrzykowski[1], K. Ulaczyk[1,2], R. Poleski[1], S. Kozłowski[1], P. Pietrukowicz[1], P. Mróz[1,3], K. Rybicki[1], P. Iwanek[1], M. Wrona[1], and M. Gromadzki[1]

[1] Astronomical Observatory, University of Warsaw, Aleje Ujazdowskie 4, 00-478 Warszawa, Poland; dszczyg@astrouw.edu.pl
[2] Department of Physics, University of Warwick, Gibbet Hill Road, Coventry, CV4 7AL, UK
[3] Division of Physics, Mathematics, and Astronomy, California Institute of Technology, Pasadena, CA 91125, USA

Received 2020 June 4; revised 2020 October 31; accepted 2020 November 9; published 2021 February 1

Abstract

We present the most extensive and detailed reddening maps of the Magellanic Clouds (MCs) derived from the color properties of Red Clump (RC) stars. The analysis is based on the deep photometric maps from the fourth phase of the Optical Gravitational Lensing Experiment (OGLE-IV), covering approximately 670 $\deg^2$ of the sky in the Magellanic System region. The resulting maps provide reddening information for 180 $\deg^2$ in the Large Magellanic Cloud (LMC) and 75 $\deg^2$ in the Small Magellanic Cloud (SMC), with a resolution of $1\farcm7 \times 1\farcm7$ in the central parts of the MCs, decreasing to approximately $27' \times 27'$ in the outskirts. The mean reddening is $E(V-I) = 0.100 \pm 0.043$ mag in the LMC and $E(V-I) = 0.047 \pm 0.025$ mag in the SMC. We refine methods of calculating the RC color to obtain the highest possible accuracy of reddening maps based on RC stars. Using spectroscopy of red giants, we find the metallicity gradient in both MCs, which causes a slight decrease of the intrinsic RC color with distance from the galaxy center of ~0.002 mag/deg in the LMC and between 0.003 and 0.009 mag/deg in the SMC. The central values of the intrinsic RC color are 0.886 and 0.877 mag in the LMC and SMC, respectively. The reddening map of the MCs is available both in downloadable form and as an interactive interface.

Unified Astronomy Thesaurus concepts: Interstellar dust extinction (837); Magellanic Clouds (990); Red giant clump (1370)

Supporting material: data behind figure, machine-readable table

1. Introduction

The Large and Small Magellanic Clouds (LMC and SMC, respectively) are a pair of irregular galaxies that, due to their proximity to the Milky Way (MW) and their mutual interactions, are the most studied nearby galaxies. They serve as a local laboratory for investigating galaxy structure, evolution, and interactions, as well as stellar populations and interstellar medium distribution. The Magellanic Clouds (MCs) are also used to calibrate the cosmological distance scale.

The majority of stellar population studies require accounting for interstellar extinction in order to acquire precise distances; thus, it is very important to have accurate reddening maps of the Magellanic System. Previous efforts to construct reddening maps employed various tracers such as Red Clump (RC) stars (Udalski et al. 1999a, 1999b; Subramaniam 2005; Subramanian & Subramaniam 2009, 2013; Haschke et al. 2011; Tatton et al. 2013; Choi et al. 2018; Górski et al. 2020), classical Cepheids (Inno et al. 2016; Joshi & Panchal 2019), or RR Lyrae–type variables (Pejcha & Stanek 2009; Haschke et al. 2011; Deb 2017). Interstellar reddening has also been inferred from equivalent widths of spectral lines (Munari & Zwitter 1997), stellar atmosphere fitting (Zaritsky et al. 2002, 2004), and through the analysis of spectral energy distributions of background galaxies (Bell et al. 2019).

RC stars are low-mass red giants in the core He-burning stage of the evolution that occupy a well-defined region in the color–magnitude diagram (CMD). This property allows for these stars to be used as standard candles for determining distances (Paczyński & Stanek 1998) and by measuring shifts between the observed and theoretical RC color, can be successfully used to measure reddening to these stars. For details on RC stars and their applications with possible limitations, see the review by Girardi (2016).

In this study, we present the most detailed and extensive reddening maps of the MCs to date, based on RC stars. Section 2 provides details on observations and data preparation. In Section 3, we describe the process of determining RC color, and in Section 4, we analyze the intrinsic RC color distribution in the MCs. Section 5 describes the final reddening maps and compares them with previous reddening maps of the MCs. We summarize the paper in Section 6.

2. Observations and Data Preparation

2.1. OGLE-IV Observations

The 1.3 m telescope of the OGLE survey is located at the Las Campanas Observatory in Chile and has been observing the southern sky since 1996 on a nightly basis. The fourth phase of the project started in 2010, when a new 32 chip mosaic CCD camera with a 1.4 $\deg^2$ total field of view was installed on the telescope. Since then, OGLE-IV has been observing the Magellanic System in the I and V bands with a cadence of 1–4 days, later reduced to about 10 days in the sparsely populated regions of the Magellanic Bridge and the outskirts of the MCs. The OGLE-IV fields covering approximately 670 $\deg^2$ in the Magellanic System are pictured in Figure 1. For technical details on the OGLE-IV survey, please refer to Udalski et al. (2015).

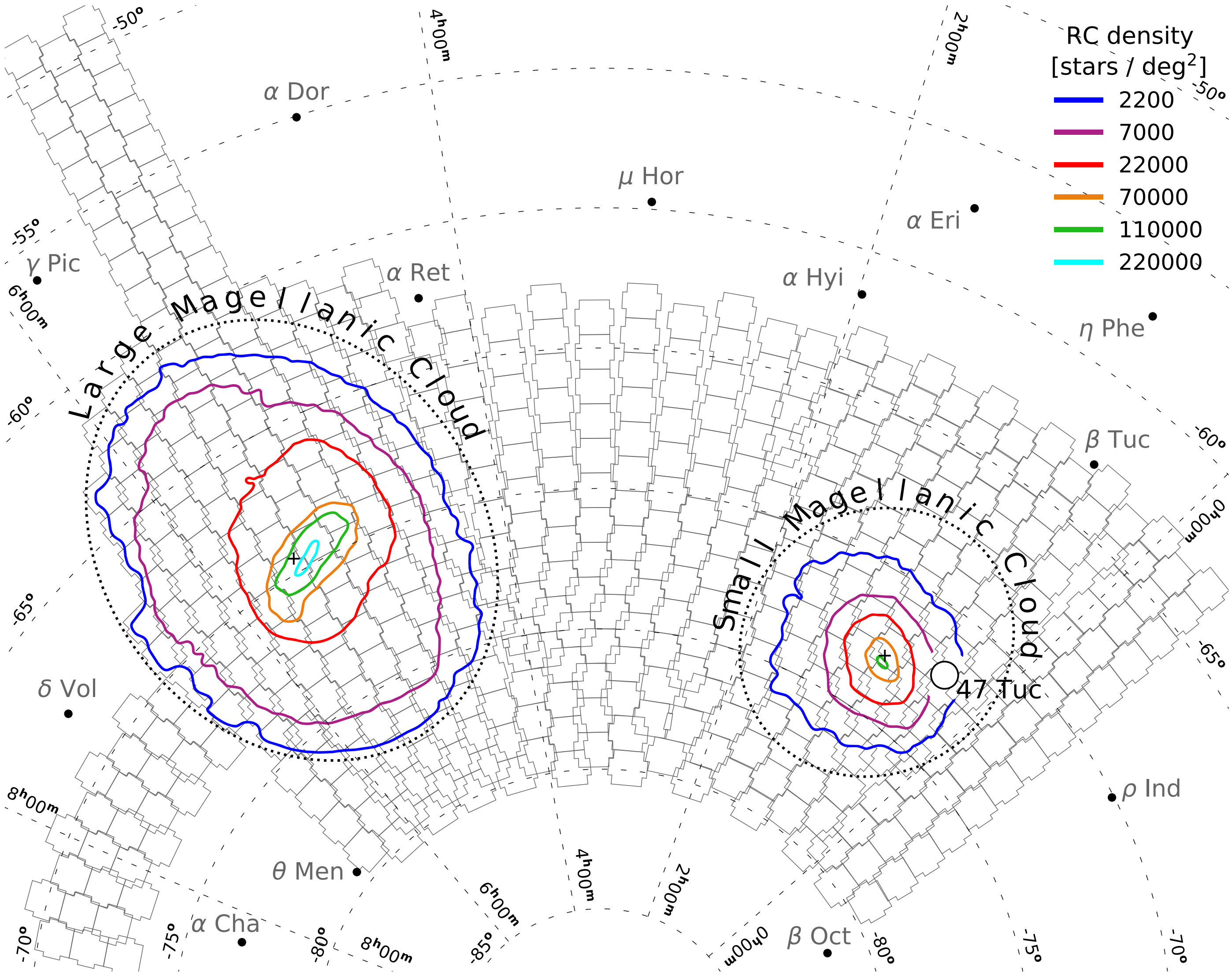

Figure 1. OGLE-IV fields in the Magellanic Clouds region (approximately 670 deg^2 of the sky, 1.4 deg^2 camera field of view), marked with gray polygons. Colored contours show densities of RC stars. The lowest density contour (blue line) in the eastern part of the LMC is affected by the edge of the OGLE footprint. Black crosses mark centers of the galaxies adopted throughout this paper: ($05^h29^m00^s$, $-68°30'00''$) from van der Marel (2001) for the LMC and ($00^h52^m12\overset{s}{.}5$, $-72°49'43''$) from de Vaucouleurs & Freeman (1972) for the SMC.

The magnitude range of regular OGLE-IV images is 12–21 mag in the *I* band and 12.5–21.5 mag in the *V* band. In order to increase the effective depth of the survey, deep OGLE-IV images were constructed from 2 to 100 high-quality frames (depending on the field), with a median of 8 images in the *V* band and 88 in the *I* band. The resulting magnitude limit of the deep images is approximately 23 mag in the *I* band and 23.5 mag in the *V* band. Even though the use of the deep images is not necessary for this particular study, because the mean magnitude of RC stars in the MCs is much brighter than the regular survey limit, it is useful due to their cleanness—stacking multiple images removes practically all artifacts and spurious detections from the final frame, which are hard to fully account for otherwise (see discussion in Skowron et al. 2014).

2.2. Data Preparation

Observational data were reduced with a standard OGLE reduction pipeline, and photometry was carried out with an image subtraction pipeline as described in Udalski et al. (2015). Each of the 32 CCD chips is 2048 × 4096 pixels, but the size of the photometric map of that chip is slightly larger (about 2200 × 4496 pixels) due to small telescope shifts between pointings. For the same reason, star counts on the chip edges are lower than in the main parts of the chip. In order to ensure high data completeness, we removed about 50 pixels on each side of the map in the x direction and about 100 pixels on each side in the y direction. The cut was determined individually for each field and chip by finding a deviation from the median star counts across the frame. After these cuts, many frames still had an overlapping region, so in the next step, the duplicate entries were removed from overlapping chips.

The Magellanic System is rich in globular and open clusters. We removed all clusters listed in the catalog of the Magellanic System clusters (Bica et al. 2008) and in the OGLE Collection of of Star Clusters (Sitek et al. 2016, 2017) from the final sample, using the mean value of both dimensions as a cluster diameter.

Finally, we transformed the data from the equatorial coordinates (α, δ) to Cartesian (x, y) coordinates using a

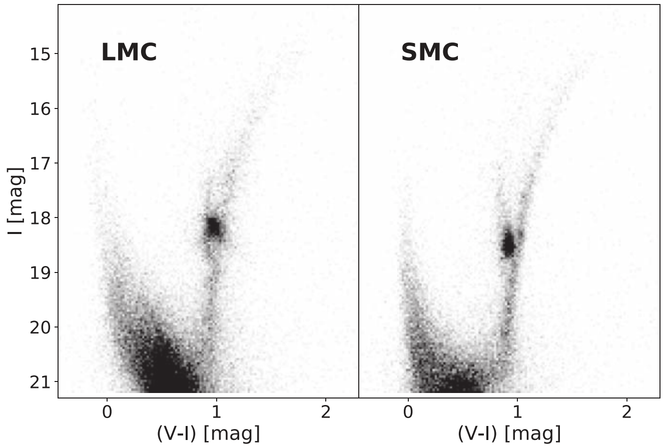

Figure 2. Hess diagrams for a typical field in the LMC (left) and the SMC (right), with a well visible RC and the RGB. The binning is 0.04 mag in magnitude and 0.02 mag in color.

Hammer equal-area projection (Snyder 1993) centered at $\alpha_c = 3.3$ h and $\delta_c = -70°$. The data were then subdivided into square regions using six bin sizes: x, $y = 0.032$, 0.016, 0.008, 0.004, 0.002, 0.001, corresponding to areas of approximately 3.34, 0.83, 0.21, 0.052, 0.013, 0.003 $\deg^2$, respectively. Varying the subfield size is useful for increasing the resolution in the central parts of the MCs and decreasing it in the outskirts, where the star counts are low. In other words, we created six different maps of the Magellanic System, where each map has a different resolution. We then repeated the process after shifting centers of the square regions by half the bin size in both the x and y directions. As a result, the number of regions in each map has increased fourfold, thus further improving the final resolution.

3. Determining the Red Clump Color

For each subfield (and in each of the six subfield sizes), we construct a $(V - I, I)$ CMD and bin it in both magnitude and color to obtain a Hess diagram, using bin sizes of 0.04 and 0.02 mag in I and $V - I$, respectively. The value of each bin is the number of stars that fell into that bin. Figure 2 shows an example of the Hess diagram in the LMC (left) and in the SMC (right), with a well visible RC and the red giant branch (RGB). The location of the RC on the CMD depends on distance and metallicity, and so it is different for the two galaxies. The elongation of the RC in the SMC has been known for a long time (Hatzidimitriou & Hawkins 1989; Udalski et al. 2008b), and it has been shown that it is caused by the large depth of the SMC along the line of sight, rather than a presence of blue-loop stars (Nidever et al. 2013).

The first step in determining the RC color is to define the initial CMD region occupied by RC stars, which will be used for a more detailed analysis. Its location and extent change with extinction—the more reddened the region, the more dispersed and shifted toward fainter magnitudes and redder colors the RC is. There are two main approaches: (a) to define a generous CMD region, which would cover all possible RC locations, and deal with disentangling the RC in a subsequent algorithm; and (b) to define a small box in $(V - I)$ and magnitude and modify its position and size iteratively (or by hand) for each line of sight, and then use a simple algorithm such as a mean or median to calculate the final RC color. The disadvantage of the first approach is that the contamination from other stars within the region forces the algorithm to be much more complex. However, in the second approach, in order to remove the majority of contamination (e.g., the RGB) and outliers (from the MW foreground), one has to reduce the size of the box and potentially remove some of the genuine RC stars. This leads to biases in the final measurement.

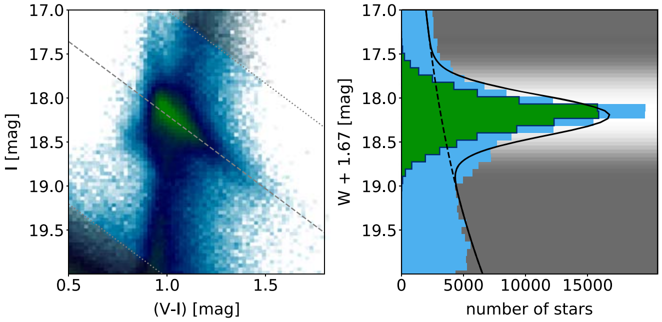

Figure 3. Hess diagram for a typical moderately reddened field in the LMC (left panel) with a well-defined RC. Gray dotted lines mark the slanted CMD region that is used for determining a luminosity function, and the dashed line shows the subsequently estimated peak of the RC distribution in W (defined as $I - 1.67\ (V - I)$). The magnitude histogram from the entire slanted region (right panel) is shown in blue. The black solid line is the fit to the histogram ($\mathrm{LF} = \mathrm{LF}_{\mathrm{RC}} + \mathrm{LF}_{\mathrm{RGB}}$), while a dashed line is the RGB component ($\mathrm{LF}_{\mathrm{RGB}}$). The white, shaded band represents the probability ($p_{\mathrm{LF}} = \mathrm{LF}_{\mathrm{RC}}/\mathrm{LF}$) of belonging to the RC, while the green histogram is that probability multiplied by the blue histogram, i.e., it can be interpreted as a magnitude distribution of RC stars.

Within the discussed scenarios, the box can be "rectangular" or "slanted", i.e., the CMD region can be defined only by specifying a range in color and magnitude, or it can follow the extinction vector. In the second case, the area of the box can be safely reduced, which in effect lowers the contamination from the RGB stars. We see no obvious disadvantages of the latter choice, which can be simply viewed as a definition of the magnitude axis using a Wesenheit index (W).

In this study we choose the generous CMD region approach and the "slanted" magnitudes (left panel of Figure 3):

$$W = I - 1.67\,(V - I\,) \quad \text{for LMC}, \tag{1}$$

$$W = I - 1.74\,(V - I\,) \quad \text{for SMC}. \tag{2}$$

We restrict our investigation to a conservative range in color of $0.65 < (V - I) < 1.7$ mag and a magnitude range that falls within $17 < I < 20$ mag at $(V - I) \approx 1$, which is typical for the RC. In the center of the LMC, due to the large differential reddening, we extend the color range to $(V - I) = 2.1$ mag. In our approach, the final results are not sensitive to the exact choice of the extinction slope and magnitude range.

First, we determine a luminosity function of the RC in W, which is fairly narrow (typical dispersion of 0.23 mag) even for highly extincted fields. There are two main components in the luminosity function: a distinct distribution of stars belonging to the RC and a smooth contribution of the RGB. The first is well approximated by the Gaussian distribution and the second can be modeled with an exponent or, in this narrow magnitude range, even with a straight line (see the right panel of Figure 3). Our aim is not to make a precise model of the luminosity function but to determine the most likely region in W where the RC stars are located, and then, with the measurement of the standard deviation, assign the probability of belonging to the RC for each star.

We tested various fitting scenarios, in particular the normal distribution plus the exponent, and found that the biggest obstacle in determining the RC magnitude region is the unstable nature of the fits in regions with lower star counts. Concurrently, we noticed that the scale parameter of the exponent is rather consistent between various lines of sight. Hence, the exact value of this parameter is not crucial, and we decide to fix it to 2.5 mag, which makes the fits more stable. The luminosity function then becomes

$$\begin{aligned} \mathrm{LF}(W) &= \mathrm{LF}_{\mathrm{RC}}(W) + \mathrm{LF}_{\mathrm{RGB}}(W) \\ &\sim \exp\left(-\frac{1}{2}\left(\frac{W-\overline{W}}{\sigma_W}\right)^2\right) + A\exp\left(\frac{W}{2.5}\right), \end{aligned} \quad (3)$$

where $\overline{W}$ is the mean, σ_W is the standard deviation of the Gaussian, and A reflects the relative amplitudes of the two components. The luminosity function is marked with a black solid line in the right panel of Figure 3.

In the second step, we fit the $(V-I)$ distribution where we weigh each star with its probability of belonging to the RC sample based on the luminosity function:

$$p_{\mathrm{LF}}(W) = \mathrm{LF}_{\mathrm{RC}}(W)/\mathrm{LF}(W). \quad (4)$$

This approach is analogous to choosing a box in magnitude W but avoids imposing sharp limits, which could bias the RC sample, or conversely, leave too many unrelated stars within the sample. Even though this approach minimizes the contamination of the RGB in the RC sample, it does not remove it completely—there is still an RGB component visible in the color distribution. The majority of MC regions have moderate differential reddening, and both components can be well approximated using the normal distribution $\mathcal{N}(\overline{V-I}, \sigma)$ (see upper panels of Figure 4).

In order to properly model the RC color distribution in all lines of sight, even those with a large differential reddening, we expand the basic model of $\mathcal{N}(\overline{V-I}, \sigma)$ by allowing the σ parameter to be different for the low (L) and high (H) side of $\overline{V-I}$:

$$\mathcal{N}_2(\overline{V-I}, \sigma_{\mathrm{L}}, \sigma_{\mathrm{H}}) = \begin{cases} \dfrac{2\sigma_{\mathrm{L}}}{\sigma_{\mathrm{L}}+\sigma_{\mathrm{H}}}\mathcal{N}(\overline{V-I}, \sigma_{\mathrm{L}}), & \text{for } (V-I) < \overline{V-I} \\ \dfrac{2\sigma_{\mathrm{H}}}{\sigma_{\mathrm{L}}+\sigma_{\mathrm{H}}}\mathcal{N}(\overline{V-I}, \sigma_{\mathrm{H}}), & \text{for } (V-I) > \overline{V-I} \end{cases}. \quad (5)$$

This modification was introduced after the visual inspection of hundreds of fields with various models of the color fit. The most typical situation in the inner parts of the MCs is that some fraction of stars lie between the observer and the bulk of dust—this fraction has a characteristic color scatter of σ_{L}. The rest of the stars lie within or behind the dust and are affected by the differential reddening, and for these stars, a better approximation is to use a different, higher value of σ_{H}. Such a hybrid model also allows for a reasonable approximation of many atypical RC distributions, but at the same time defaults to a Gaussian-like profile for the majority of well-behaved lines of sight. Figure 5 presents four examples of atypical RC color distributions, where this hybrid model ($\mathcal{N}_2$) proves useful.

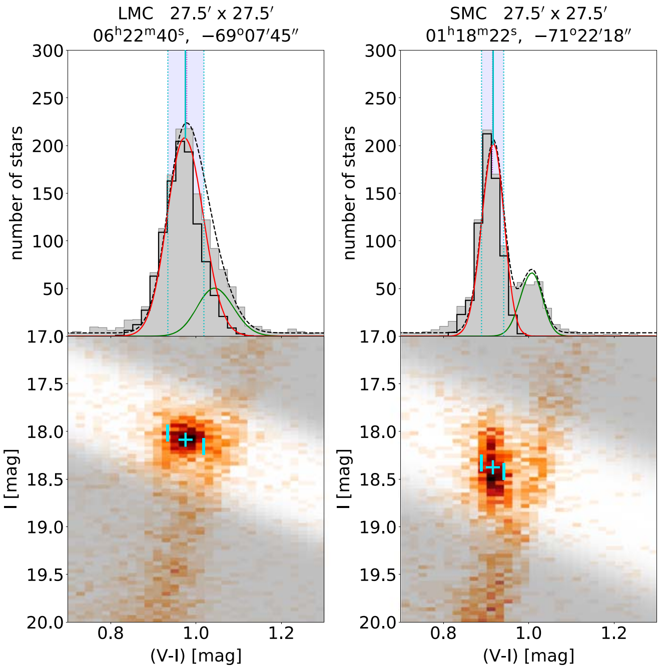

Figure 4. Color distribution in the RC region for a typical field in the LMC (left) and the SMC (right). Gray histograms in top panels show the distribution of stars suspected to lie within the RC region based on the luminosity function fit (histogram of all stars times the probability $p_{\mathrm{LF}}(W)$). The dashed black line marks the whole model $f(V-I)$ fitted to the distribution, while the red and green lines show the RC and RGB components, respectively. The cyan vertical line is the median of the RC component only, and the blue band marks the 68% interval. The black histogram presents the final RC sample, where the gray histogram is multiplied by the probability based on the components of the fit $p_{\mathrm{RC}}(V-I)$. The pink dashed line marks the mode value of the RC color sample. Bottom panels show Hess diagrams of the regions where the cyan cross marks the median of the fitted RC color distribution, and cyan lines correspond to the ±34% intervals adopted from the upper panels.

In general, Gaussian fitting is very sensitive to outliers, which can introduce a large bias in the fit parameters. Here we model the outliers with the constant background component added to the components of the RC and the RGB. Our model in principle has eight parameters: $(\overline{V-I})_{\mathrm{RC}}$, $(\overline{V-I})_{\mathrm{RGB}}$, four σ components (L and H, for both RC and RGB), and A_{RGB} and A_{BKG}, where the last two parameters are the relative amplitudes of the RGB to RC and the background to the RC, respectively. Fitting of such model to the data is inherently unstable because the RGB and RC regions overlap. Also the number of parameters is too large for many areas with low star counts. But because we are interested in determining the color of the RC only, and the RC component is dominant, we can determine other fit parameters approximately. This is sufficient to reduce the impact of the RGB and the MW foreground on the RC and reduces the systematic error of the RC color measurement. In order to do so, we fix the color offset between the RGB and RC, i.e., we fix $O_{\mathrm{RGB,RC}} = (\overline{V-I})_{\mathrm{RGB}} - (\overline{V-I})_{\mathrm{RC}}$ to 0.07 in the LMC and 0.09 in the SMC. These values were determined with a simple algorithm that estimates the RGB color at the RC brightness using a ±1 magnitude range around the RC (with the narrow $\pm 2\,\sigma_W$ region around the RC magnitude removed). In other words, the algorithm uses parts of the RGB immediately above and below the RC. It then measures the median RGB color in 0.2 mag (or no less than 50 stars) bins, and using a linear fit, estimates the median RGB color at the RC position. The reported color offsets between the median RC and RGB colors ($O_{\mathrm{RGB,RC}}$) are practically constant

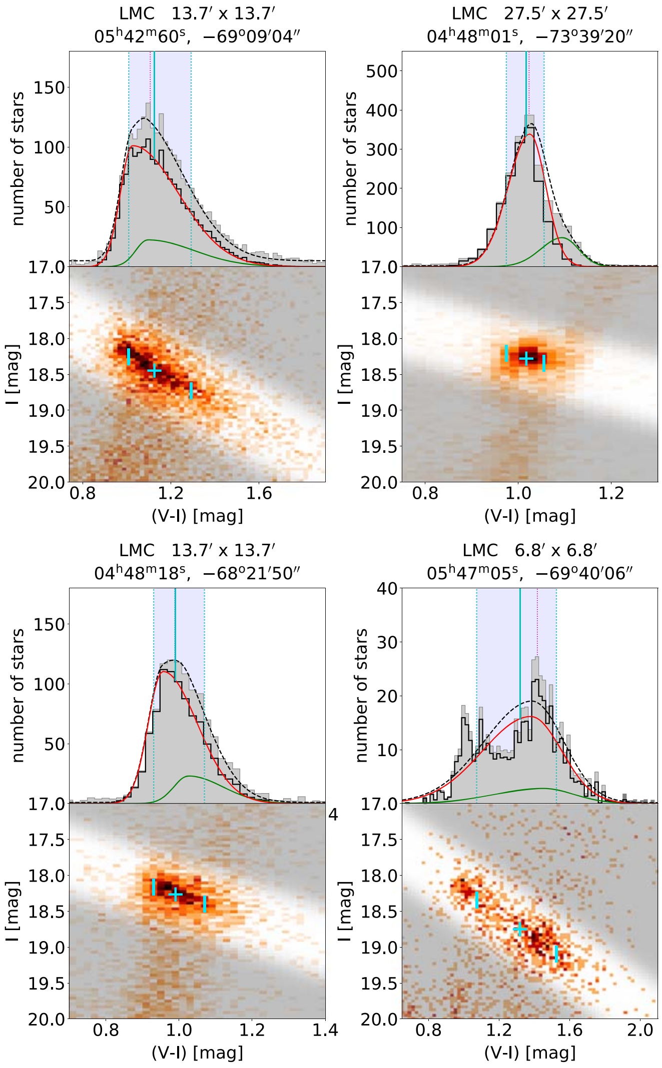

Figure 5. Color distribution in the RC region for sample LMC fields with non-Gaussian fits to the RC and RGB distributions. Lines and symbols are analogous to those in Figure 4. The combined distribution function ($f(V-I)$, dashed gray) consists of a constant background term plus RC and RGB contributions described by the $\mathcal{N}_2(V-I)$ model shifted by 0.07.

across the galaxies, with a typical scatter of 0.01 mag. In order to assess how such scatter influences the measured RC color, we performed RC color calculations with $O_{\rm RGB,RC}$ changed by −0.01 mag and +0.01 mag and found that it causes only a −0.001 mag and +0.001 mag difference, respectively, in the calculated RC color. This shows, that assuming a constant RGB-RC color offset in the entire galaxy is reasonable, especially when other sources of error are an order of magnitude larger.

We also found that it is sufficient to use a single width of the Gaussian components for the RC and the RGB ($\sigma_{\rm L,RGB} = \sigma_{\rm L,RC}$ and $\sigma_{\rm H,RGB} = \sigma_{\rm H,RC}$) to model the observed distribution, as a higher differential reddening affects both groups of stars in the same way. This was verified by comparing standard deviations of the RC and RGB distributions in all LMC and SMC sight lines. They are equal to within a few percent.

Finally, we optimize the algorithm by estimating the relative number of stars within the RGB and RC groups in the previous step by integrating the RGB luminosity function with appropriate weights ($p_{\rm LF}(W) \times {\rm LF}_{\rm RGB}(W)$).

The four-parameter model:

$$\begin{aligned} & f((\overline{V-I})_{\rm RC}, \sigma_{\rm L}, \sigma_{\rm H}, A_{\rm BKG})(V-I) \\ & \quad = f_{\rm RC}(V-I) + f_{\rm RGB}(V-I) + f_{\rm BKG}(V-I) \\ & f_{\rm RC}(V-I) = \mathcal{N}_2((\overline{V-I})_{\rm RC}, \sigma_{\rm L}, \sigma_{\rm H})(V-I) \\ & f_{\rm RGB}(V-I) = A_{\rm RGB}\, \mathcal{N}_2((\overline{V-I})_{\rm RC} \\ & \quad + O_{\rm RGB,RC}, \sigma_{\rm L}, \sigma_{\rm H})(V-I) \\ & f_{\rm BKG}(V-I) = A_{\rm BKG} \end{aligned} \tag{6}$$

(where $A_{\rm RGB}$ is calculated from the LF and $O_{\rm RGB,RC}$ is fixed) is fitted to the color distribution of stars expected to lie within the RC region based on the luminosity function fit, i.e., to the distribution of all stars multiplied by the probability $p_{\rm LF}(W)$.

We calculate a median value (50th percentile) of the first component of the fitted model ($f_{\rm RC}$, representing only the RC distribution), as well as ±34.1% intervals from the median, as an analog of a typical σ value of a Gaussian distribution, providing the final color estimation as

$$\text{median}(V-I)^{+\sigma_2}_{-\sigma_1} = \text{median}(V-I)^{\text{centile}(50+34.1)-\text{median}}_{\text{centile}(50-34.1)-\text{median}}. \tag{7}$$

The probability that a given star belongs to the RC sample can be assessed with

$$p_{\rm RC}(V-I) = f_{\rm RC}(V-I)/f(V-I). \tag{8}$$

The black histograms in Figures 4 and 5 show the final RC sample. The mode of the histogram (or the most likely color value) is equal to the median for symmetric Gaussian profiles and is typically smaller for asymmetric profiles, because for the majority of lines of sight, the differential reddening makes $\sigma_{\rm H} > \sigma_{\rm L}$. We estimate the modal value by fitting a constant level with a small Gaussian bump to the final RC sample, across the entire color range. The mean and sigma of the Gaussian component are fitted, but the area under the Gaussian is fixed and set to one-sixth of the total area of the model. That way, we avoid noise in the mode, which is typically imposed by arbitrary binning. In the final table, we provide both the median and the mode of the RC color distribution and leave it to the user to decide which is more suitable for their needs. One can imagine that depending on the scientific question asked, either the mode or the median reddening for a given line of sight will give a better answer. However, in the subsequent analysis, we will use the median RC color and hence the median reddening value. We also provide ±34.1% percentile values from the median as a measure of confidence intervals and of differential reddening.

Previous studies of reddening in the Magellanic Clouds typically used a combination of a Gaussian and a polynomial to fit the RC distribution (e.g., Haschke et al. 2011; Choi et al. 2018; Górski et al. 2020). However, this has a tendency to miss the RGB contamination entirely and focus the polynomial on the smooth stellar background instead. In effect, in fields with low differential reddening, this overestimates the RC color due to the RGB contamination, and in fields with high differential reddening, it chooses the most likely value. Additionally, in regions with lower star counts—either in the outskirts of the galaxies or in areas with large reddening, a simpler fit (with fewer parameters) is generally more stable because it does not

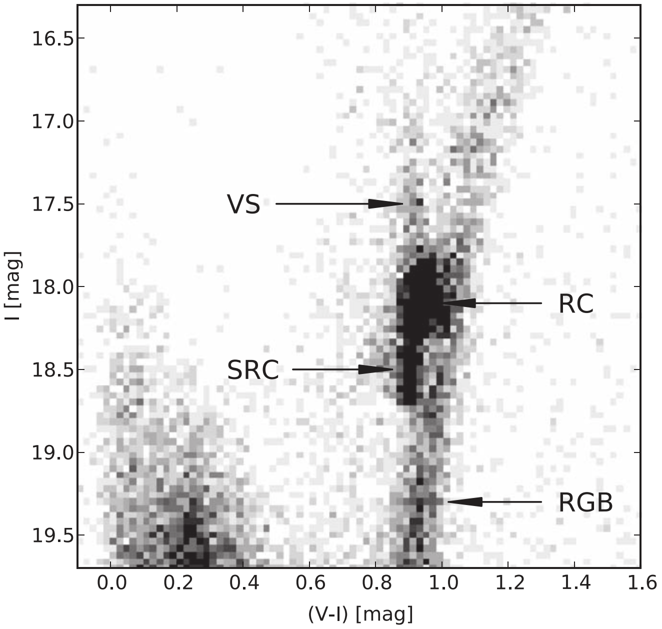

Figure 6. A Hess diagram of a $27'.5 \times 27'.5$ area in the LMC (centered at $\alpha = 05{:}30{:}52$, $\delta = -63{:}49{:}12$) showing an example of the complexity of the RC. The marked structures are the main RC, the secondary RC (SRC), and the vertical structure (VS).

require a large number of stars to converge. This allows for retaining high resolution in such areas.

3.1. The Age-related Complexity of the Red Clump

The RC observed in some parts of the LMC is rich in various substructures: a distinct secondary RC (SRC), which is about 0.4 mag fainter and slightly bluer than the main RC and is composed of younger, ~1 Gyr stars (Girardi 1999); a vertical structure (VS), which is made of brighter and more massive RC stars; and a horizontal branch (HB) composed of low-mass metal-poor stars at the same evolutionary stage (see the review by Girardi 2016). Figure 6 shows an example of these substructures in one of many such sight lines in the LMC. The SRC is the second most pronounced feature in the CMD, and its origin is well depicted in Figure 11 of Girardi (2016), which shows the age structure of RC stars—the younger the stars within the 1–2 Gyr range, the bluer they are. Also, as shown in Figure 6 of Girardi (2016), their luminosity varies by ~0.5 mag within this age range, which is the reason why the SRC is elongated in magnitude. However, for stars older than 2–3 Gyr, both magnitude and color change very slightly with age (see Figure 1 of Girardi & Salaris 2001), resulting in a very compact RC. In other words, the $(V - I)$ of older RC stars remains almost constant with age.

The presence of the SRC and/or VS significantly widens the observed distribution of RC stars in magnitude (σ_W) and influences our estimation of the number of stars in the RC ($N_{\rm RC}$) based on the LF. In order to trace regions of the LMC where these additional structures are visible, we calculate the $N_{\rm RC}/N$ parameter, which is the relative number of RC stars to all stars in the ±1 mag range around the measured RC brightness ($W_{\rm RC}$). In other words, it is the ratio of the number of stars in the green histogram to the number of stars in the blue histogram shown in the right panel of Figure 3, but limited to the ±1 mag range around $W_{\rm RC}$. In regions where this parameter is above ~50%, we observe the additional RC structures, which are significant enough, that may influence the color measurement of the older, main RC. The two-dimensional distribution of $N_{\rm RC}/N$ is shown in Figure 7 and will be discussed in detail in a forthcoming paper (J. Skowron et al. 2021, in preparation).

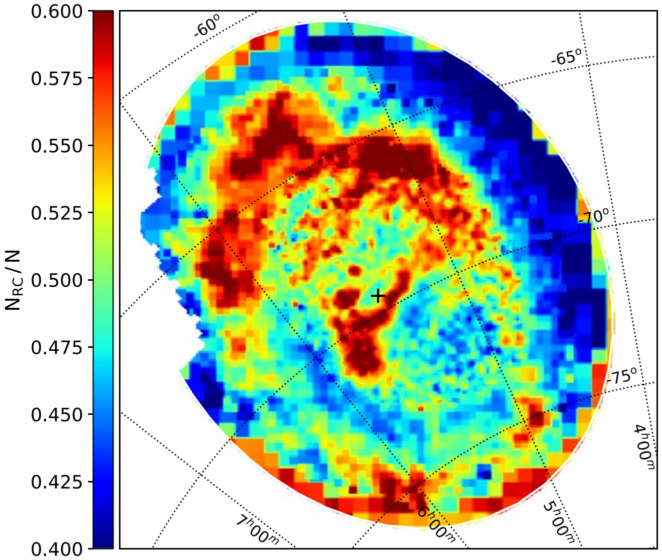

Figure 7. The two-dimensional distribution of $N_{\rm RC}/N$—the relative number of RC stars to all stars in the ±1 mag range around the measured RC brightness, in the LMC. The detailed discussion of the observed distribution will be presented in J. Skowron et al. (2021, in preparation).

The presence of an additional young (<2 Gyr) RC population, whose intrinsic color is bluer by a couple of hundredths of a magnitude (~0.04 mag) than that of a regular RC, has an effect on the measurement of $(V - I)$. The resulting offset is of the order of 0.01 mag and depends on the relative number of the young to old RC population. Because the regular RC is more numerous and its intrinsic color is more stable across the galaxy, we decide to use only the regular, older RC to derive the reddening. The detailed modeling of a complex RC structure, including a star formation history, would be a very challenging task itself and is beyond the scope of this paper. However, the influence of the young RC on the measured color of the main RC can be estimated empirically using the $N_{\rm RC}/N$ parameter as a proxy for the severity of the effect, and this is done in Section 4.

In the SMC, the RC is largely elongated in magnitude. Some of this dispersion may be explained by the RC age and metallicity distribution (Girardi 1999), although the majority of this effect is caused by a large depth of the SMC along the line of sight, rather than population effects (Nidever et al. 2013). Hence, even though the distribution of $N_{\rm RC}/N$ is not entirely uniform throughout this galaxy, this is caused mainly by geometrical, not population, effects and does not need to be taken into account.

3.2. Discussion of (V − I) Uncertainties

The uncertainties for a single OGLE photometric measurement are small (about 0.005 mag in the I band and 0.008 in the V band at the RC magnitude) and because those measurements are averaged for at least 80 stars to obtain the RC color measurement for each line of sight, their individual errors have a negligible effect ($\lesssim$0.001 mag).

The accuracy of our final $(V - I)$ color of the RC is a combination of three factors. The field-to-field systematic calibration errors of the OGLE photometry are of the order of 0.01 mag (Udalski et al. 2015). The second source of error is associated with fitting the RC distribution and estimating the median. In order to assess the error of calculating the median color, we performed a number of simulations, where 50,000 star samples were generated from the model f (Equation (6)), with a varying number of stars and a varying differential reddening parameter. We then processed these artificial samples in the exact same way as the real data and estimated the median color of the RC. The resulting error was from about 0.001 mag for samples containing 500–1000 stars and with a small spread in RC color ($\sigma \sim 0.02$–0.04 mag), to about 0.008 mag for samples containing only 80–200 stars and having a large spread in RC color ($\sigma \sim 0.07$–0.09 mag). The typical error of the median RC color across the galaxies (averaged for all lines of sight) is 0.0035 mag and 0.0031 mag, in the LMC and SMC, respectively.

The third source of uncertainty in estimating $(V - I)$ is the difference between the assumed model of the color distribution and the actual distribution of stars—the intrinsic shape of the RC and RGB populations does not necessarily follow a simple Gaussian profile, but it changes with the star formation history and metallicity distribution. However, the dominant difference comes from the complex nature of dust clouds in any given field and the relative position of stars and dust clouds along the line of sight. Our σ_1 and σ_2 parameters are indicative of the variability of the reddening in a given field. These are also our best estimations of the uncertainty of the reddening value toward a given star. In the majority of the MCs, σ_1 and σ_2 are typically between 0.03 and 0.05 mag. In the centers, they are of the order of 0.10 mag, reaching 0.30 mag in the dustiest regions of the LMC.

In summary, the errors of estimating the median $(V - I)$ in regions with low σ values are not greater than the systematic uncertainties of the photometry, while with the growing values of σ, the uncertainty of estimating the median becomes less and less relevant. Nevertheless, we can provide an upper bound on the error of our estimations for the majority of the studied area. In Sections 4.2 and 4.3, we measure the scatter between our median reddening values and values interpolated from the reddening maps of Schlegel et al. (1998) in the outer parts of both galaxies. We find the scatter of 0.014 mag in the LMC and 0.018 mag in the SMC in all lines of sight outside of the central regions. These values encapsulate all sources of error from both our and the Schlegel et al. (1998) study, as well as other systematic problems, such as the mismatch of the spatial resolution between the two studies, the assumptions about the intrinsic color of the RC, and the reddening law used to transform reddening values between different passbands.

4. Determining the $(V - I)_0$ of the Red Clump

The intrinsic color of the RC depends on both age and metallicity (Girardi & Salaris 2001). The widely used reddening maps of Haschke et al. (2011) adopted a theoretical value of 0.92 mag and 0.89 mag for $(V - I)_0$ in the center of the LMC and SMC, respectively. Górski et al. (2020) measured $(V - I)_0 = 0.838$ mag for the LMC and $(V - I)_0 = 0.814$ mag for the SMC, which are a mean of four distinct methods. Nataf et al. (2020) employed a hybrid theoretical and empirical approach and derived $(V - I)_0 = \{0.89, 0.92, 0.88\}$ mag for the LMC, using three different methods, and $(V - I)_0 = \{0.84, 0.84\}$ mag for the SMC. All of the above studies were limited to the inner parts of the MCs and assumed a constant metallicity, and thus the RC color value.

In order to determine the intrinsic unreddened $(V - I)_0$ color of the RC in the MCs, we correct the median measured $(V - I)$ values for the foreground dust of the MW, for which we use the all-sky reddening map of Schlegel et al. (1998) based on dust infrared emission (hereafter SFD). The map provides $E(B - V)$ values that can be converted to $E(V - I)$, taking into account the recalibration of the SFD dust map by Schlafly & Finkbeiner (2011). The recalibration recommends a 14% decrease of $E(B - V)$ and the use of the $R_V = 3.1$ Fitzpatrick (1999) reddening law. We use the convenient conversion coefficients provided by Schlafly & Finkbeiner (2011):

$$A_V / E(B - V)_{\mathrm{SFD,original}} = 2.742 \tag{9}$$

$$A_I / E(B - V)_{\mathrm{SFD,original}} = 1.505 \tag{10}$$

that give

$$E(V - I)_{\mathrm{SFD}} = A_V - A_I = 1.237\, E(B - V)_{\mathrm{SFD,original}}. \tag{11}$$

The SFD galactic reddening map is shown in Figure 8(a). The dust temperature and reddening values in the LMC and SMC centers are not reliable because their temperature structure is not sufficiently resolved (Schlegel et al. 1998), therefore we cut out the central regions of the MCs from further analysis of $(V - I)_0$. In the case of the LMC, we remove the inner $4\overset{\circ}{.}1$ radius circle centered at $(05^{\mathrm{h}}20^{\mathrm{m}}00^{\mathrm{s}}, -68°48'00'')$. This region contains the inner disk of the LMC, which is abundant in gas, dust, and young stars. The dust content is clearly seen in SFD emission maps (Figure 8(a)) and will be apparent in our maps of differential reddening. The majority of Classical Cepheids in the LMC (Jacyszyn-Dobrzeniecka et al. 2016) are located in this region (with a sharp decline in density outside). This is also the center of rotation of H I gas measured using the 21 cm line (de Vaucouleurs 1960) and was also shown to be an acceptable center for the optical rotation curve (Feast et al. 1961). Thus, we adopt this "radio center" coordinates as a center of the excluded region, which is offset by over 1° from the LMC optical disk center at $(05^{\mathrm{h}}29^{\mathrm{m}}00^{\mathrm{s}}, -68°30'00'')$ from van der Marel (2001).

In the case of the SMC, we remove measurements within an ellipse centered at $(00^{\mathrm{h}}58^{\mathrm{m}}00^{\mathrm{s}}, -72°12'00'')$, which was selected by eye to encompass the affected central region of the galaxy ($r_a = 2\overset{\circ}{.}0$, $r_b = 1\overset{\circ}{.}3$, $r_{\mathrm{PA}} = 40°$) and is also different from the optical center of the SMC at $(00^{\mathrm{h}}52^{\mathrm{m}}12\overset{\mathrm{s}}{.}5, -72°49'43'')$ from de Vaucouleurs & Freeman (1972). See black circle/ellipse in Figure 8, with their centers marked with black dots and optical centers marked with crosses.

The middle panel of Figure 8 shows the median $(V - I)$ colors of the RC in the MCs measured in this work, while panel (c) shows the RC colors corrected for the MW reddening (the difference between panels (a) and (b)), i.e., the intrinsic color $(V - I)_0$. Once again, it is clear that SFD reddening values within the central regions of the MCs are not real and only the values outside the marked areas can be used to determine the intrinsic color of the RC. Panels (b) and (c) also illustrate that the outskirts of the galaxies (the areas outside white ellipses) are not suitable for determining $(V - I)_0$—the color determination in these regions is erratic and the visual investigation of color fits in these lines of sight confirms that

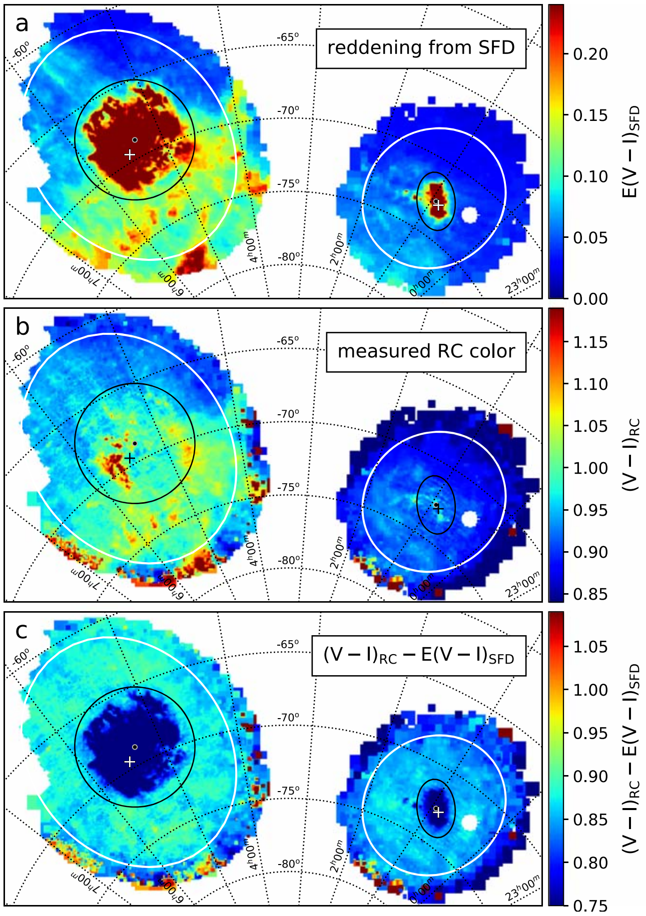

Figure 8. The comparison of SFD reddening in the MCs' area with RC color measured in this work. Panel (a) shows the Galactic reddening map from SFD converted to $(V-I)$. Panel (b) presents RC color values measured in this work (median), while panel (c) shows the difference between panels (b) and (a), i.e., the RC colors corrected for the MW reddening. Central regions of the MCs, in which the SFD map is not reliable, are marked with black circle and ellipse for the LMC and SMC, respectively, while the rejected outer regions are marked with white ellipses. Black dots represent dust disk centers of the MCs, and the crosses mark the optical centers of the LMC and SMC. The empty region within the SMC is the location of the globular cluster 47 Tuc.

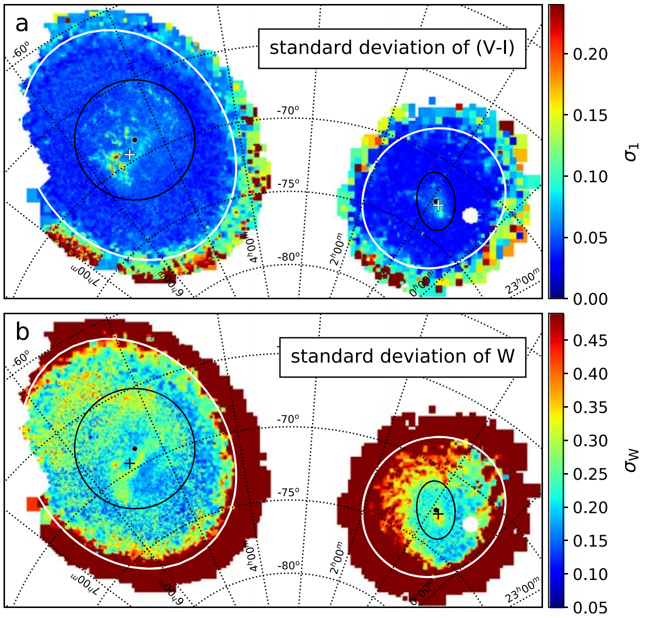

Figure 9. The scatter of RC color σ_1 (panel (a)) and the standard deviation of RC brightness σ_W (panel (b)). Central regions of the MCs, in which the SFD map cannot be used, are marked with black circle and ellipse for the LMC and SMC, respectively, while the rejected outer regions are marked with white ellipses. Black dots represent the dust disk centers of the MCs, and the crosses mark the optical centers of the LMC and SMC.

they are not reliable. The main reason is that we reach the edge of the galaxies where the RC star counts are so low that the RC is not well defined. This is well depicted in Figure 9(a), where we see a significant increase in σ_1 in the outskirts of the MCs (panel (a)). The highest values of σ_1 coincide with the increased MW extinction in the southern part of the LMC. This is caused by the reddened population of MW stars interfering with the RC of the LMC in the CMD. As a result, the region occupied by RC stars in the CMD is dominated by the MW foreground and the Gaussian fit generates a very wide peak across the entire fitting box defined in Section 3. This is also reflected in a very high value of σ_W (panel b), where the outskirts of the MCs reach $\sigma_W = 0.5$ mag, which reflects the fact that the LF is dominated by the background contamination and there is no distinct RC component visible.

We therefore assume that all measurements that fall outside the white ellipses (Figures 8 and 9) are unreliable and reject them from the intrinsic RC color analysis. The ellipses were chosen based on the surface density of RC stars—about 1000 stars deg^{-2}. Then, after visual inspection of CMDs on both sides of the ellipses, the ellipse parameters were slightly adjusted to ensure that the bad measurements are outside the ellipse, while the majority of the good ones fall inside the ellipse.

As discussed in Section 3.1, there is a bias in the measurement of the $(V-I)$ of the RC in some parts of the LMC that is caused by the presence of additional RC structures, mainly the younger SRC. The additional, bluer SRC is composed of stars younger than about 2 Gyr, while the majority of RC stars are older, and their intrinsic color $(V-I)_0$ remains fairly constant with age. Figure 7 shows the distribution of $N_{\rm RC}/N$ that reveals sight lines, where the measured $(V-I)$ is affected by the young SRC. Figure 10 shows how our measurement of the intrinsic color is as a result biased with the growing value of $N_{\rm RC}/N$. Even though the color difference between the regular RC and the SRC is a few hundredths of a magnitude, typically ~0.04 mag, its influence on the measured color is on average only of the order of 0.01 mag. We apply this small correction $(0.1 \times (N_{\rm RC}/N - 0.5)$ for $N_{\rm RC}/N \geqslant 0.5)$ to the final value of $(V-I)$, based on Figure 10. The detailed modeling of the RC in individual sight lines is not necessary, because the correction is small compared to other sources of uncertainty.

4.1. Metallicity Gradient in the MCs

As was already discussed, the RC color depends on both the age and metallicity of the RC. Because we are using only the intermediate- and old-age RC stars (approximately >2–3 Gyr), the color change with age is negligible in this age range, but the change with metallicity is not (Figure 1 of Girardi & Salaris 2001).

The presence of the metallicity gradient in the LMC has long been a subject of discussion (Choudhury et al. 2016 and references therein), although recent studies support a shallow

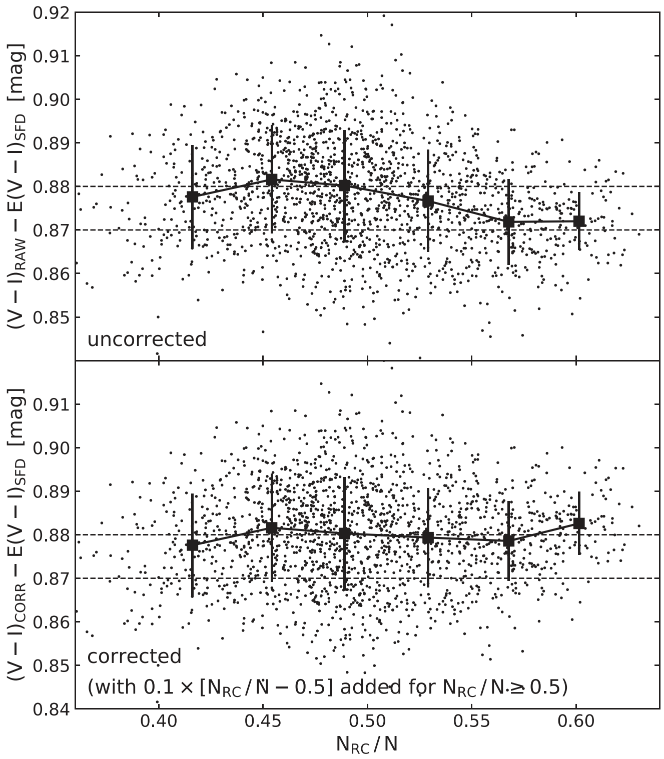

Figure 10. The dependence of the measured RC color on $N_{\rm RC}/N$. The top panel shows the change of our measured intrinsic color $(V-I)_0 = (V-I)_{\rm RC} - E(V-I)_{\rm SFD}$ with the growing contribution of the SRC to the total RC. The mean change is not more than 0.01 mag. The bottom panel shows the above corrected for the presence of the SRC, according to the simple straight line fit as written in the panel.

metallicity gradient, e.g., -0.047 ± 0.003 dex kpc^{-1} out to ∼8 kpc (Cioni 2009), -0.029 ± 0.002 dex kpc^{-1} in the inner 5 kpc (Skowron et al. 2016), and from -0.049 ± 0.002 to -0.066 ± 0.006 dex kpc^{-1} up to a radius of 4 kpc (Choudhury et al. 2016). The distribution of [Fe/H] among the LMC clusters also shows a radial dependence (Pieres et al. 2016).

In the case of the SMC, the existence of the metallicity gradient has also been questioned, although a number of most recent results do report a shallow metallicity gradient: -0.075 ± 0.011 dex/deg within the inner 5° (Dobbie et al. 2014), -0.08 ± 0.08 dex/deg out to 4° (Parisi et al. 2016), from -0.045 ± 0.004 to -0.067 ± 0.006 dex/deg within the radius of $2\overset{\circ}{.}5$ (Choudhury et al. 2018), and -0.031 ± 0.005 within the inner 2° (Choudhury et al. 2020).

Nataf et al. (2020) used [Fe/H] metallicities of bright and faint red giants, derived by the ASPCAP pipeline (García Pérez et al. 2016) from high-resolution spectra taken for the APOGEE survey (Majewski et al. 2017), which is part of the Sloan Digital Sky Survey (Blanton et al. 2017), and found a mean metallicity value for the inner LMC [Fe/H] = −0.64 dex (within the inner LMC disk, i.e., inside the black circle), and [Fe/H] = −0.88 dex for the inner SMC. Following Nataf et al. (2020), we select bright and faint red giants ($K > 12.25$ mag and $0.55 < J - K < 1.3$ mag) as defined by Nidever et al. (2020), from APOGEE LMC fields 1–17, encompassing both the central parts and the outskirts of the LMC, and from SMC APOGEE fields 1–7 (see their Figure 1). We then remove foreground stars ($\log(g) \geqslant 2$) and very metal-poor stars ([Fe/H] $\leqslant -1.3$ dex in the LMC and [Fe/H] $\leqslant -1.6$ dex in the SMC). This leaves 2134 red giants in the LMC and 957 in the SMC. Their distribution is shown in Figures 11(a) and (b), for the LMC and SMC, respectively, and their metallicity values against distance from the LMC/SMC optical center are plotted in panels (c) and (d). In the case of the SMC, we adopt an elliptical system with the major to minor axis ratio of 1.5 and a position angle of $55\overset{\circ}{.}3$ east of north, in order to account for the elongation of the SMC and to be consistent with previous metallicity studies (e.g., Piatti et al. 2007; Dobbie et al. 2014; Parisi et al. 2016). The line fit to the data gives a metallicity gradient of -0.026 ± 0.002 dex deg^{-1} in the LMC. In the majority of the SMC, the gradient is consistent with -0.033 ± 0.005 dex deg^{-1}, but there is a clear change in the slope at about $1\overset{\circ}{.}5$ distance (in elliptical coordinates), and the gradient can be described by -0.118 ± 0.027 dex deg^{-1} in the central part of the SMC.

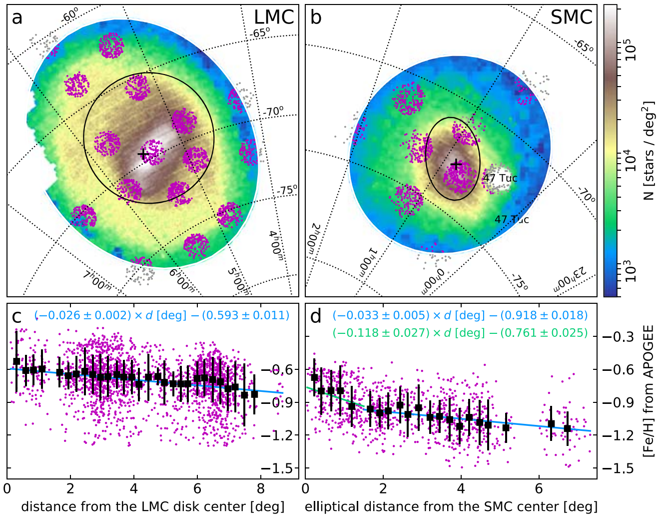

Figure 11. The sample of red giants from APOGEE MCs fields (Nidever et al. 2020). Panels (a) and (b) show their distribution on top of the density maps of OGLE-IV giants, for the LMC and SMC, respectively. Panels (c) and (d) show how spectroscopically determined [Fe/H] values change with the distance from the center of the LMC and SMC, respectively. The blue line in the bottom panels is the line fit to the data. Black squares mark the binned data.

Because the locations of the APOGEE fields are sparse across the galaxies and the scatter of [Fe/H] values is large, it is difficult to investigate the metallicity gradient in more detail, i.e., to verify whether it is uniform in all radial directions. However, if the metallicity gradient was variable, it would not significantly alter the results of this paper due to a very shallow dependence of $(V-I)_0$ on [Fe/H] within the metallicity range of the MCs, which is discussed below.

The relation between the intrinsic color of the RC and its metallicity is supported by both theory and observations (Girardi 2016; Nataf et al. 2020). In an attempt to calibrate this dependence, we selected a sample of 17 star clusters from the LMC and SMC, which are older than 3 Gyr and younger than 9.5 Gyr, as their RC color does not change with age over this age range (see Figure 1 of Girardi & Salaris 2001). The selection also required that the clusters are located in areas with low reddening ($E(V-I)_{\rm SFD} < 0.12$ mag). We use their [Fe/H] values available in the literature (Da Costa & Hatzidimitriou 1998; Bica et al. 1998; Grocholski et al. 2006; Glatt et al. 2008; Parisi et al. 2009; Dias et al. 2016), with the preference for spectroscopically determined metallicities over the photometric ones, if both were available. The spectroscopically determined

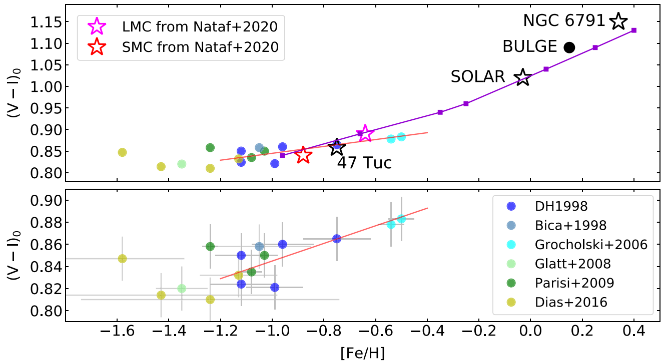

Figure 12. The dependence of the intrinsic RC color on metallicity. The bottom panel is a close-up of the top panel to show the measurement uncertainties in the metallicity range considered in this work. The cluster metallicity data are for clusters older than 3 Gyr and younger than 9.5 Gyr on the Carretta & Gratton (1997) metallicity scale. The data are from Da Costa & Hatzidimitriou (1998), Bica et al. (1998), Grocholski et al. (2006), Glatt et al. (2008), Parisi et al. (2009), and Dias et al. (2016). The intrinsic RC color for all the above is based on OGLE-IV data. Both [Fe/H] and $(V-I)_0$ for 47 Tuc, the solar neighborhood, and NGC 6791 are from Nataf et al. (2020) and are marked with black stars (see their Figure 1 for comparison). The data for the Galactic Bulge are from Bensby et al. (2017). For comparison, the results from Nataf et al. (2020) for the LMC and SMC are marked with pink and red stars, respectively. The purple line is the theoretical relation from Nataf et al. (2020) shifted by −0.03 mag (see their Section 2.4). The red line shows a line fit for $-1.2 < \mathrm{[Fe/H]} < -0.4$ dex, which accounts for both [Fe/H] and $(V-I)_0$ uncertainties, with the slope of 0.080 ± 0.016 mag dex^{-1} and the zero point of 0.925 ± 0.016 mag.

metallicities are based on the calcium triplet technique and have typical uncertainties of ~0.05 dex. The photometric estimations are based on comparing the observed and synthetic CMDs and have much larger errors, usually >0.20 dex. The RC colors of the 17 clusters are measured using OGLE-IV data within the cluster radius, with a typical error <0.02 mag, and dereddened with the SFD maps. Because MC star clusters meeting these criteria are rather metal poor, we supplement the above data set with data for NGC 6791 and the solar neighborhood (Nataf et al. 2020) and for the Galactic Bulge (Bensby et al. 2017).

Figure 12 shows the dependence of the intrinsic RC color $(V-I)_0$ on metallicity [Fe/H] for the above sample. The top panel includes the theoretical relation between $(V-I)_0$ and [Fe/H] from Nataf et al. (2020), which was limited to $\mathrm{[Fe/H]} \sim -1.0$ dex at the low-metallicity end (the purple line). The red line shows a line fit to the data points, within the metallicity range considered in this work ($-1.2 < \mathrm{[Fe/H]} < -0.4$ dex). The estimated slope is 0.080 ± 0.016 mag dex^{-1} and the zero point is 0.925 ± 0.016 mag. The fit takes into account both [Fe/H] and $(V-I)_0$ uncertainties, marked in the bottom panel of Figure 12. The intrinsic color change in this metallicity range is nonnegligible but small, and the estimated slope may change with the availability of new cluster data. The calculated slope of 0.08 mag dex^{-1}, combined with the metallicity gradient[4] in both galaxies (as estimated in Figure 11), predicts an intrinsic color change with the distance from the galaxy center of the order of −0.002 mag deg^{-1} in the LMC, −0.003 mag deg^{-1} in the outer SMC, and −0.009 mag deg^{-1} in the inner SMC.

4.2. $(V-I)_0$ of the Red Clump in the LMC

The distribution of $E(V-I)_{\mathrm{SFD}}$ reddening in the MW around the LMC is presented again in Figure 13(a), while panel (b) shows the distribution of the unreddened RC color, i.e., the difference between the measured median $(V-I)$ color of RC and the $E(V-I)_{\mathrm{SFD}}$ reddening in the MW around the LMC. The MW dust distribution in the LMC region is not uniform—its southern part is highly affected by dust, the northeastern part is moderately affected, whereas the northwestern part is almost unaffected by Galactic extinction. We therefore subdivide the LMC into four quadrants (Figure 13, panels (a)–(b)), along constant R.A. and decl., that cross in the center of the LMC disk ($05^{\mathrm{h}}29^{\mathrm{m}}00^{\mathrm{s}}$, $-68°30'00''$, from van der Marel 2001). Note that the center of dust emission is offset from the center of the LMC disk by over one degree. Each of Figures 13(c)–(f) contains three plots: the MW reddening $E(V-I)_{\mathrm{SFD}}$ (top, blue points), the measured median RC color $(V-I)$ (middle, red points) and their difference, i.e., the inferred intrinsic RC color $(V-I)_0 = (V-I) - E(V-I)_{\mathrm{SFD}}$ (bottom, cyan points), against the distance from the center of the LMC disk. They represent data within the four quadrants of the LMC: northeast (panel (c)), northwest (panel (d)), southeast (panel (e)), and southwest (panel (f)). Black points in all plots show spurious measurements that either fall inside the black circle (where $E(V-I)_{\mathrm{SFD}}$ is wrong) or outside the white ellipse (where RC color measurements are spurious) pictured in panels (a) and (b). The dark-gray shaded area marks the central region entirely excluded from the analysis, while the light-gray shaded area marks the region partially excluded from the analysis (the black circle crosses a range of distances due to the difference in coordinates of the LMC dust and stellar disks).

The line fit to $(V-I)_0$ versus distance from the LMC center (cyan points) is shown with a dashed line in the bottom plots of panels (c)–(f). The fit is based on joined data from the NE, SE, and SW quadrants and accounts for the fixed metallicity gradient and the resulting RC color change of −0.002 mag deg^{-1}. The different behavior of $(V-I)_0$ in the NW is unlikely to be caused by the actual intrinsic color difference in this LMC quadrant but is very likely to be a systematic effect originating from the calibration of SFD extinction maps. This effect becomes most prominent in LMC regions with the lowest MW extinction, probably because the contribution of the LMC internal dust is higher than that of the MW foreground dust, for which the relation between dust temperature and reddening was calibrated. Another possibility is that $E(V-I)_{\mathrm{SFD}}$ is underestimated in regions with very low dust density. For these reasons, we did not use the NW quadrant, where the reddening is the lowest, when fitting the intrinsic color.

The median value of $(V-I)_0$ in the investigated area, between the black circle and the white ellipse, is 0.877 mag. The scatter of individual lines of sight around the fitted line is 0.014 mag. The predicted intrinsic color in the LMC center from the color gradient is 0.886 mag, which is consistent with the results of Nataf et al. (2020).

4.3. $(V-I)_0$ of the Red Clump in the SMC

The MW extinction around the SMC is lower, and its distribution is more uniform than around the LMC (see Figure 14(a)), with only a slight difference between the MW dust distribution in the northern and southern parts of the SMC. The distribution of the unreddened RC color, i.e., the difference

---

[4] There is an offset of ~0.06 dex between the metallicity scale of APOGEE and of Carretta et al. (Nidever et al. 2020), but it is not relevant for this study as we are only using the slope of the relation, not the zero point.

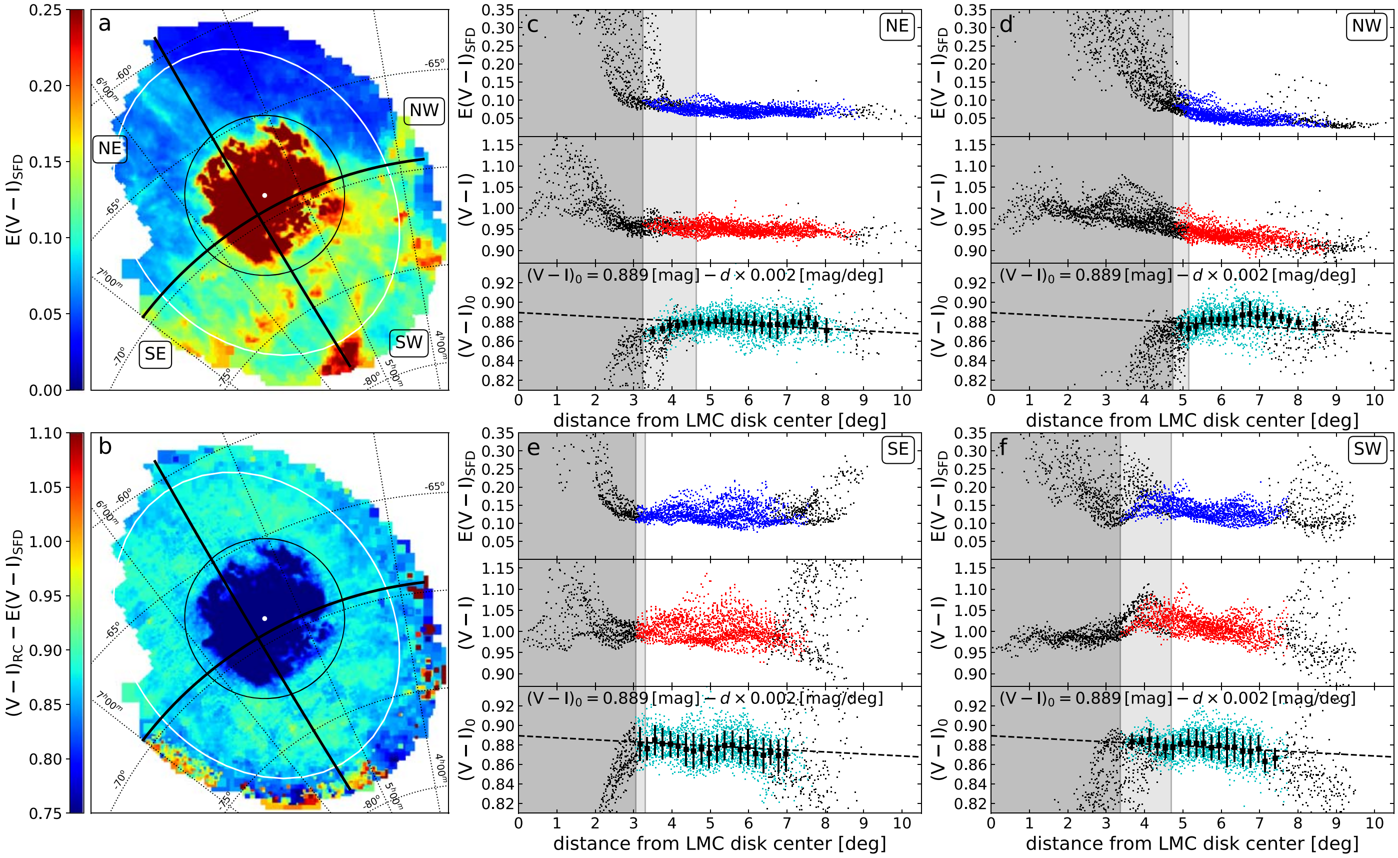

Figure 13. The intrinsic color of the RC in the LMC. The distribution of $E(V-I)_{\rm SFD}$ MW reddening in the LMC is shown in panel (a), while the difference between the measured $(V-I)$ color of the RC and the MW reddening is shown in panel (b). The circle marks the area excluded from the analysis of $(V-I)_0$ and is centered at the LMC center of rotation in radio and optical marked with a white dot (Feast et al. 1961). The black solid lines of constant R.A. and decl. cross at the center of the LMC disk (van der Marel 2001) and subdivide the LMC disk into four regions: northeast, northwest, southeast, southwest. Panels (c)–(f) represent data for the four quadrants of the LMC, as marked in panel (a). Each of panels (c)–(f) is composed of three plots: the MW reddening $E(V-I)_{\rm SFD}$ (top, blue points), the measured RC color $(V-I)$ (middle, red points), and their difference, i.e., the inferred intrinsic RC color $(V-I)_0$ (bottom, cyan points), against the distance from the LMC disk center. The dark-gray shaded area marks the central region excluded entirely from the analysis, while the light-gray shaded area marks the region partially excluded from the analysis (the black circle crosses a range of distances because it is centered at different coordinates). Colored points represent valid data, while black points show data excluded from the analysis. Black squares with error bars (bottom plots in panels (c)–(f)) mark median $(V-I)_0$ values and their standard deviations within bins of $0\overset{\circ}{.}2$. The black dashed line represents a fit to cyan points that accounts for the fixed metallicity gradient taken from panel (c) of Figure 11.

between the measured median $(V-I)$ color of RC and the $E(V-I)_{\rm SFD}$ reddening in the MW around the SMC is presented in Figure 14(b). Similarly to the case of the LMC, panel (c) shows the MW reddening $E(V-I)$ (top, blue points), the measured RC color $(V-I)$ (middle, red points) and the inferred intrinsic RC color $(V-I)_0$ (bottom, cyan points) against the elliptical distance from the center of the SMC at $(00^{\rm h}52^{\rm m}12\overset{\rm s}{.}5, -72^\circ49'43'')$ from de Vaucouleurs & Freeman (1972), with the major to minor ellipse axis ratio of 1.5 and a position angle of $55\overset{\circ}{.}3$ east of north (e.g., Piatti et al. 2007; Dobbie et al. 2014; Parisi et al. 2016). Black points in all plots of panel (c) show spurious measurements that either fall inside the black ellipse (where $E(V-I)_{\rm SFD}$ is wrong) or outside the white ellipse (where RC color measurements are spurious) pictured in panels (a) and (b). The dark-gray shaded area marks the central region entirely excluded from the analysis, while the light-gray shaded area marks the region partially excluded from the analysis (the black ellipse crosses a range of distances from the SMC center).

The line fit to $(V-I)_0$ versus elliptical distance from the SMC center (cyan points) is shown in the bottom plot of panel (c) with a dashed line. The fit accounts for the fixed metallicity gradient and the resulting RC color change of -0.003 mag deg^{-1} for distances larger than $\sim1\overset{\circ}{.}5$ (black line) and -0.009 mag deg^{-1} for distances smaller than $\sim1\overset{\circ}{.}5$ (orange line).

The median value of $(V-I)_0$ in the investigated area, between the black and white ellipses, is 0.853 mag. The scatter of individual measurements around the fitted line is 0.018 mag. The predicted intrinsic color in the SMC center is 0.877 mag, which is much higher than the 0.84 mag estimated by Nataf et al. (2020) and is a result of the steepening of the metallicity gradient in the inner SMC. If we assumed that the gradient does not change and follows the black dashed line (panel (c) of Figure 14), then the predicted intrinsic color in the SMC center would be 0.865 mag. Another reason for the high central value of $(V-I)_0$ may be due to the underestimation of $E(V-I)_{\rm SFD}$ in areas with very low reddening. Similarly to the NW quadrant of the LMC, where increasing $E(V-I)_{\rm SFD}$ by a few hundredths would shift the reddening estimates to fit the $(V-I)_0$ gradient estimated from other quadrants, in the SMC (where the extinction is generally much lower than in the LMC), it would cause the lowering of $(V-I)_0$.

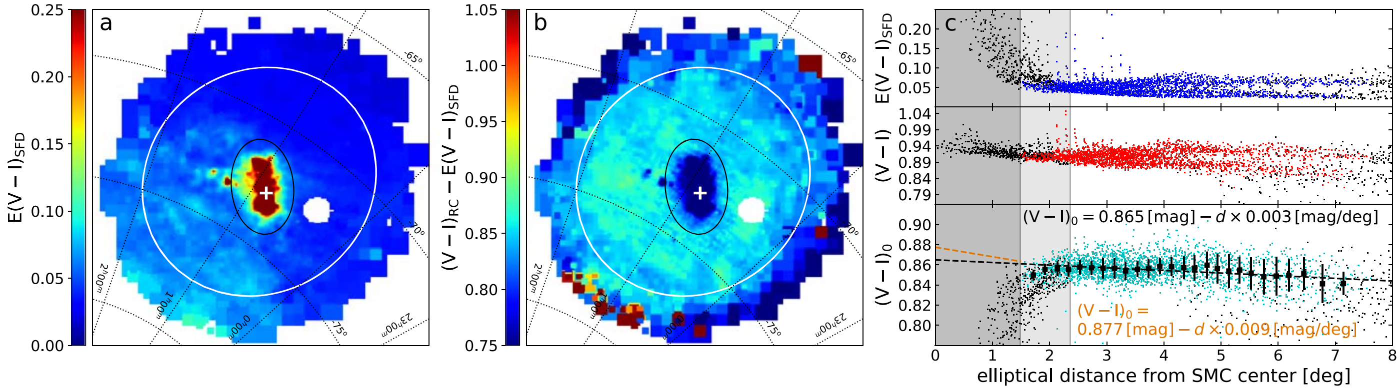

Figure 14. The intrinsic color of the RC in the SMC. The distribution of $E(V-I)_{SFD}$ MW reddening in the SMC is shown in panel (a), while the difference between the measured median $(V-I)$ color of RC and the MW reddening is shown in panel (b). The black ellipse marks the area excluded from the analysis of $(V-I)_0$. Panel (c) is composed of three plots: the MW reddening $E(V-I)_{SFD}$ (top, blue points), the measured RC color $(V-I)$ (middle, red points) and the inferred intrinsic RC color $(V-I)_0$ (bottom, cyan points) against the elliptical distance from the SMC disk center (de Vaucouleurs & Freeman 1972), marked with a cross in panel (a). The dark-gray shaded area marks the central region entirely excluded from the analysis, while the light-gray shaded area marks the region partially excluded from the analysis (the black ellipse crosses a range of distances because it is centered at different coordinates). Colored points represent valid data, while black points show data excluded from the analysis. Black squares with error bars (bottom plot in panel (c)) mark median $(V-I)_0$ values and their standard deviations within bins of $0\overset{\circ}{.}2$. The black and orange dashed lines represent a fit to cyan points that accounts for the fixed metallicity gradients from panel d of Figure 11.

5. Reddening Maps

The final $E(V-I)$ reddening map of the MCs was obtained by subtracting the intrinsic RC color (Sections 4.2 and 4.3) from the measured one. The resolution of the map is $1\overset{'}{.}7 \times 1\overset{'}{.}7$ in the central parts of the MCs and decreases down to approximately $27' \times 27'$ in the outskirts.

Figure 15 shows the distribution of reddening (panel (a)) and its standard deviation: σ_1 (panel (b)) and σ_2 (panel (c)). Both σ_1 and σ_2 are measures of internal reddening in the MCs and inform of the distribution of dust within the galaxies along the line of sight—high σ_1 indicates increased amounts of dust in the near parts, while high σ_2 in the central and far parts of the galaxy. It is well represented in panel (c), where σ_2 reflects the distribution of dust within the LMC inner disk (see Section 3 for details).

The mean reddening is $E(V-I) = 0.100 \pm 0.043$ mag in the LMC and $E(V-I) = 0.047 \pm 0.025$ mag in the SMC. This is lower than all previous measurements but is expected—this is the first reddening map of the MCs that encompasses all areas where the RC is visible, including the outskirts of the galaxies, where the reddening is very low.

The reddening data are available from http://ogle.astrouw.edu.pl/cgi-ogle/get_ms_ext.py both for download (in TEXT and FITS formats, for the users' convenience) and in the form of an interactive interface. A subset of the data is presented in Table 1.

5.1. Comparison with Previous Large-scale Reddening Maps Based on RC Stars

Here we compare our reddening maps with other large-scale reddening maps of the MCs based on RC stars. Instead of comparing reddening values themselves, which highly depend on the adopted intrinsic color of the RC, we instead compare maps of measured RC color and the adopted intrinsic RC color separately.

5.1.1. Haschke et al. (2011)

Large-scale reddening maps of the LMC and SMC published by Haschke et al. (2011) were based on RC stars from the OGLE-III data (Udalski et al. 2008a, 2008b). Authors found a mean reddening $E(V-I) = 0.09 \pm 0.07$ mag in the LMC and $E(V-I) = 0.04 \pm 0.06$ mag in the SMC. When taking into account only the area investigated by Haschke et al. (2011), we find mean reddening values of $E(V-I) = 0.122 \pm 0.048$ mag in the LMC and $E(V-I) = 0.056 \pm 0.020$ mag in the SMC. The difference is 0.032 and 0.016 mag for LMC and SMC, respectively, and is mostly a result of the adopted zero color of the RC. Haschke et al. (2011) used theoretical values that depend on metallicity, adopting $(V-I)_0 = 0.92$ mag and $(V-I)_0 = 0.89$ mag for the LMC and SMC, respectively (Girardi & Salaris 2001), while we use empirical values, which together with accounting for a metallicity gradient give mean intrinsic colors within the area investigated by Haschke et al. (2011) of $(V-I)_0 = 0.884$ (LMC) and $(V-I)_0 = 0.862$ mag (SMC).

Figure 16 presents a comparison between color measurements from this work and the work of Haschke et al. (2011). Panels (a) and (b) show a two-dimensional map of RC color differences that are color coded. The histogram of differences between $(V-I)$ color values from this work and from Haschke et al. (2011) is shown in panel (c) for the LMC and in panel (d) for the SMC. In the case of the LMC, the mean difference is $\langle (V-I)_{\rm Skowron} - (V-I)_{\rm Haschke} \rangle = -0.004 \pm 0.018$ mag. There are some expected larger discrepancies in the central region of the LMC, where the differential reddening is high, but the overall agreement is reasonable and falls within one σ value. This is further pictured in panel (e), where a comparison of color differences divided by the σ of the color is shown.

In the case of the SMC, there is a mean difference of $\langle (V-I)_{\rm Skowron} - (V-I)_{\rm Haschke} \rangle = -0.011 \pm 0.014$ mag, but there is also a systematic difference between the eastern and western parts, due to small offsets between the OGLE-III and OGLE-IV calibrations (panel (b)). As seen in panel (f), there is an agreement within one σ value for the majority of the area, although larger differences are observed at the edges, and these result from the differences in an algorithm calculating $(V-I)$.

5.1.2. Choi et al. (2018)

More recently, Choi et al. (2018) released the $E(g-i)$ reddening map of a large part of the LMC based on RC stars observed by the Survey of the MAgellanic Stellar History (SMASH; Nidever et al. 2017). They postulated that there is a

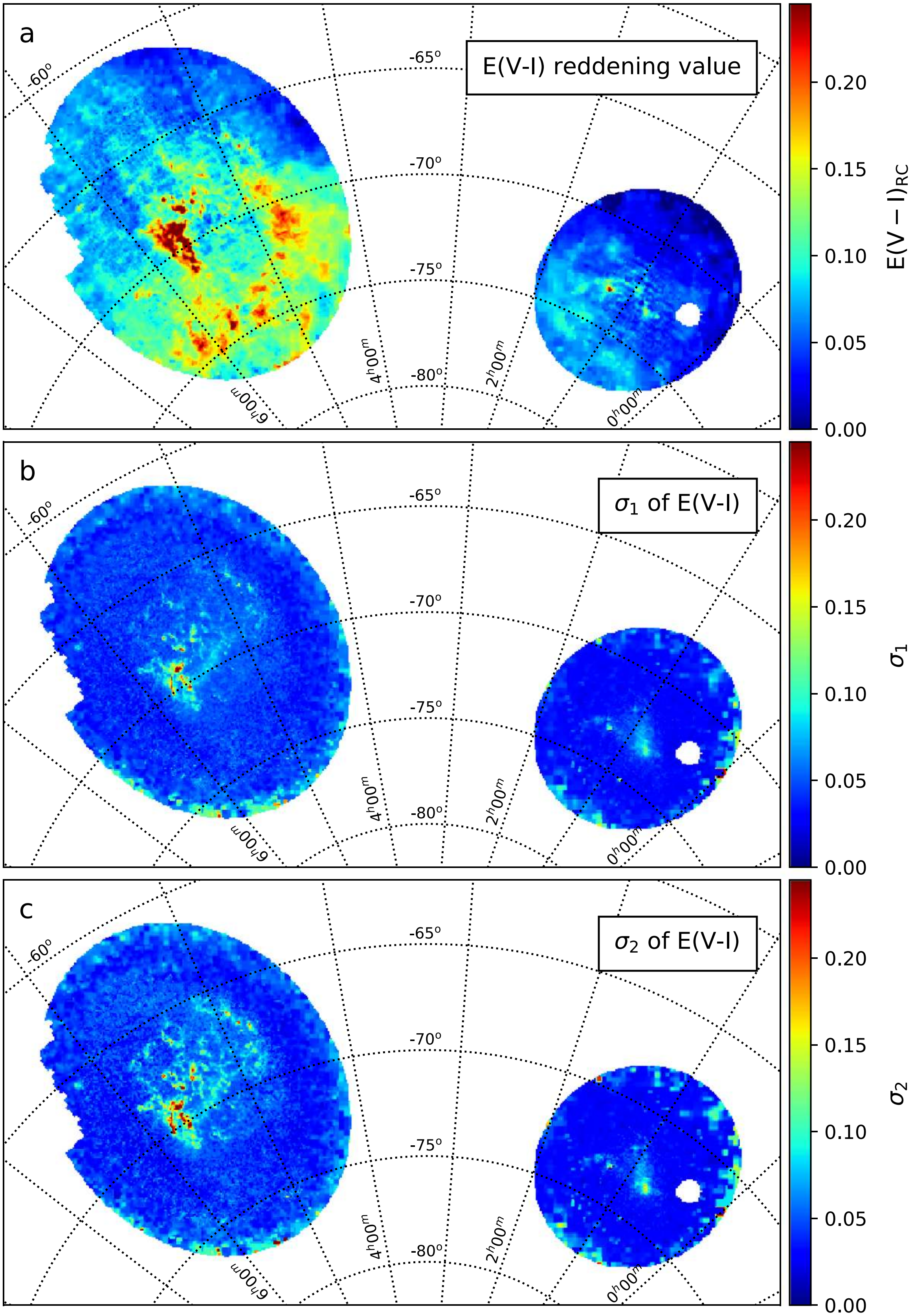

Figure 15. The reddening map of the Magellanic Clouds. Panel (a) shows the distribution of $E(V-I)$ reddening in the MCs. Panels (b) and (c) show the distribution of σ_1 and σ_2, respectively, which are an indication of the amount of dust in the near parts (σ_1) and in the central and far parts (σ_2) of the galaxies and can serve as measures of reddening uncertainties toward a single star. The empty region within the SMC is the location of the globular cluster 47 Tuc.

(The data used to create this figure are available.)

Table 1
$E(V-I)$ Reddening Map based on RC Color from the OGLE-IV Survey

R.A. (hr)	Decl. (deg)	$E(V-I)$ median	σ_1 [−34%]	σ_2 [+34%]	$(V-I)_{RC}$ median	$(V-I)_0$	$E(V-I)_{peak}$ mode	$E(V-I)_{SFD}$	Box (arcmin)
4.866824	−68.599136	0.128	0.046	0.057	1.010	0.882	0.127	0.357	3.4
5.434266	−63.469700	0.066	0.061	0.044	0.943	0.877	0.074	0.061	6.9
0.379222	−74.886131	0.039	0.030	0.028	0.896	0.857	0.042	0.041	13.8

(This table is available in its entirety in machine-readable form.)

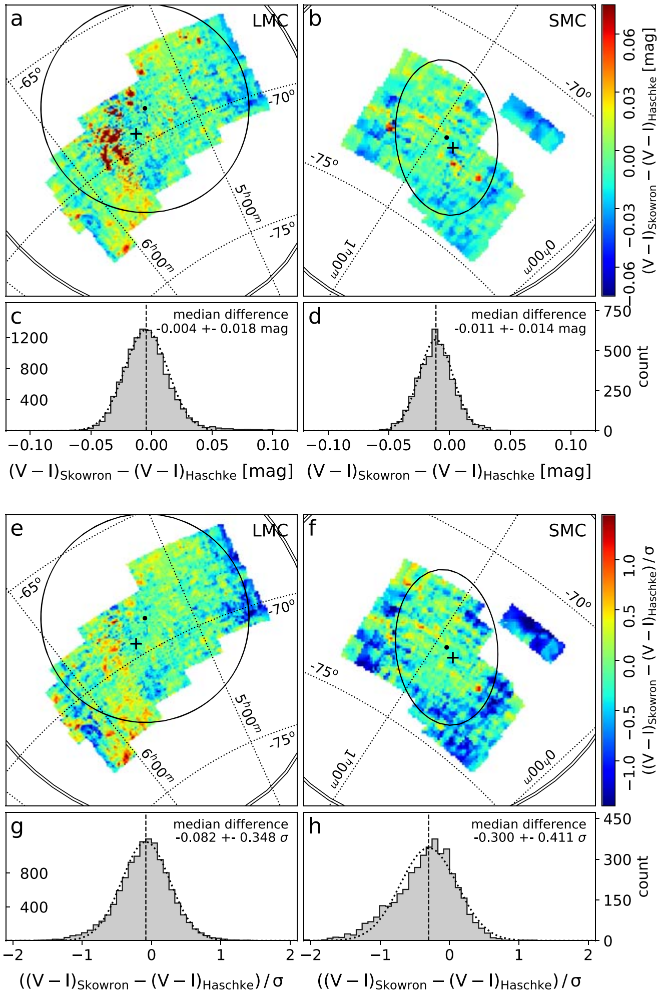

Figure 16. The comparison of color measurements from this work and the work of Haschke et al. (2011) as a two-dimensional map of RC color differences in the LMC (panel (a)) and SMC (panel (c)), and as a histogram of color differences (panels (b) and (d)). Panels (e) and (f) show the two-dimensional map of RC color differences divided by the σ of the color distribution for the LMC and SMC, respectively, while panels (g) and (h) show the corresponding histograms.

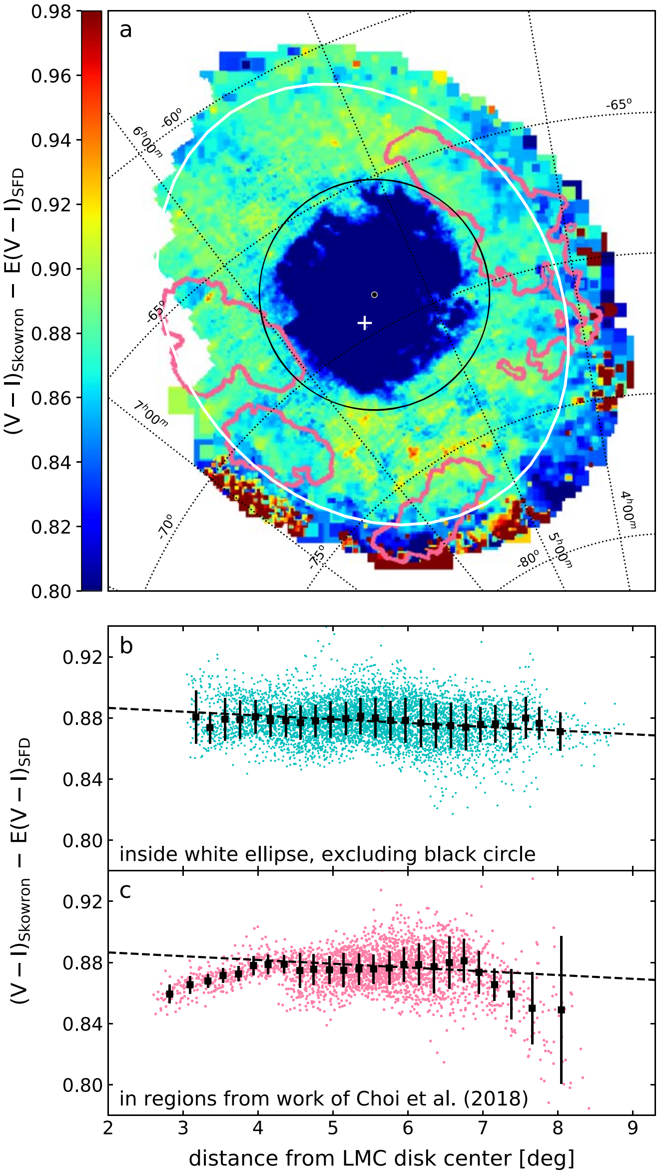

Figure 17. The $(V-I)_0$ distribution of LMC RC stars from this work is shown in panel (a). The black circle marks the central region of the LMC, where the SFD map is not reliable, while the white ellipse cuts off the rejected outer region of the galaxy, unsuitable for RC color measurements. Pink contours mark regions used by Choi et al. (2018) to determine the intrinsic RC color and are identical to their Figure 4. The plots in panels (b) and (c) show the change of $(V-I)_0$ measured in this work, with distance from the LMC disk center (white cross). Panel (b) (cyan points) shows $(V-I)_0$ in the "safe" region, between the black circle and the white ellipse, while panel (c) (pink points) shows $(V-I)_0$ within pink contours. The dashed line in panels (b) and (c) shows our derived $(V-I)_0$ gradient.

radial dependence of the intrinsic color of the RC, such that it is practically constant in the range between 4° and 7° from the galaxy center, with $(g-i)_0 = 0.822$, but follows a slope of 0.024 dex deg^{-1} between $2^{\circ}\!.7$ and 4° and a slope of −0.033 dex deg^{-1} between 7° and $8^{\circ}\!.5$ from the center of the LMC (see their Figure 7). This finding is not supported by our data. Figure 17(a) shows the distribution of $(V-I)_0$ from this work. The black circle marks the central region of the LMC, where the SFD map is not reliable, while the white ellipse cuts off the rejected outer region of the galaxy, unsuitable for color measurements. In Section 4, we demonstrated that only the region between the black circle and white ellipse can be reliably used for determining the intrinsic color of the RC. In Figure 17(a), we use pink contours to overplot regions used by Choi et al. (2018) to determine the intrinsic RC color, which are identical to their Figure 4. It can immediately be seen that the pink contours in the southern and western part of the LMC partially cover the outskirts of the LMC, where the $(V - I)$ determination is not reliable. Similarly, eastern and western contours close to the galaxy center enter the region within the black circle, in which SFD reddening values, and so the $(V - I)_0$ determination, are not realistic.

The plots in Figures 17(b) and (c) show the change of $(V - I)_0$ measured in this work, with distance from the LMC disk center. Panel (b) (cyan points) presents intrinsic color values in the "safe" region, between the black circle and the white ellipse, while panel (c) (pink points) shows the intrinsic color values within pink contours used by Choi et al. (2018). It is apparent that the $(V - I)_0$ gradient in the range $2^\circ\!.7$–4° and 7°–$8^\circ\!.5$, visible in panel (c), originates solely from the choice of regions to determine $(V - I)_0$. However, when we use data from the reliable area only, we only see a slight gradient of $(V - I)_0$ in the entire range $3^\circ\!.5$–9° from the LMC center (panel (b)), originating from the metallicity gradient in the LMC.

When working with the reddening map of Choi et al. (2018), which is provided in FITS format, we found that their map departs from the WCS convention. The FITS-WCS standard (Greisen & Calabretta 2002, Section 2.1.4) states that the "integer pixel numbers refer to the center of the pixel in each axis, so that, for example, the first pixel runs from pixel number 0.5 to pixel number 1.5 on every axis". From our tests, it appears that the reddening values of Choi et al. (2018) are for the area of the sky between the coordinates calculated for the integer pixel numbers, e.g., the first pixel represents the area between the WCS coordinates calculated for positions 1 and 2. This half-pixel offset in both axes translates to the typical offset of $7'$ in their published map and is clearly visible when comparing with our maps, especially in the center, where the resolution is $1'\!.7 \times 1'\!.7$. We account for this offset in further analysis.[5]

In order to compare RC color values from this work and from Choi et al. (2018), we use the provided $(g - i)$ color maps and transform them to $(V - I)$ with

$$(V - I)_{\rm Choi} = 0.765\,(g - i) + 0.242. \qquad (12)$$

The constant 0.242 was chosen arbitrarily so that the mean color difference is zero, as the exact value of the constant term is not known without a detailed comparison of individual stars in both samples.

In Figure 18, we plot a color-coded 2D map (panel (a)) and a histogram (panel (b)) of the differences between $(V - I)$ measured in this work and obtained by Choi et al. (2018). Panels (c) and (d) show a comparison of color differences divided by the σ of the color distribution. Even though there is a moderately good overall agreement between the two maps, there are multiple regions with significant differences, which originate from Choi et al. (2018) adopting the median value of the color distribution of all stars in the selection box, as the RC color. This is especially seen in areas with the higher scatter in color, i.e., in the center and in the outskirts. We investigated the nature of this discrepancy by looking by eye at the CMDs of regions with the largest color differences. We found that in these cases, the measurements of Choi et al. (2018) fall either on the blue or on the red side of the actual RC color peak. This is caused by the manual selection of the box containing RC stars. In the case where the RC is in the region of low extinction, their selection box omits some of the RC stars on the red side when trying to minimize the RGB contribution. This is well depicted in Figure 3 of Choi et al. (2018)—the red part of the top histogram in panel (a) is quite sharply cut off. The median of such a distribution will underestimate the real color of the RC, falling on the blue side of the maximum of the RC color histogram. In the other case, when the RC is in the region of high extinction, their selection box contains mostly all RC stars on the red side, but there is a sharp cutoff on the blue side in order not to include other features that might contain stars from different populations. (see the red part of the top histogram in Figure 3(b) of Choi et al. 2018). The median of such a distribution will overestimate the real RC color, falling on the red side of the maximum of the RC color histogram.

5.1.3. Górski et al. (2020)

Most recently, Górski et al. (2020) published an update of the reddening maps of Haschke et al. (2011) based on OGLE-III RC stars, with a new calibration of the intrinsic RC color based on independently measured reddening of late-type eclipsing binary systems and blue supergiants and reddening derived from Strömgren photometry of B-type stars. They calculated the intrinsic RC color separately for each tracer and then averaged the results to find $(V - I)_0 = 0.838 \pm 0.034$ in the LMC and $(V - I)_0 = 0.814 \pm 0.034$ in the SMC. This is disturbingly lower than the values obtained in this work. If we average our intrinsic color estimates within the region investigated by Górski et al. (2020), we obtain a mean $(V - I)_0$ of 0.883 mag for the LMC and 0.862 mag for the SMC. The difference is 0.045 and 0.048 mag for the LMC and SMC, respectively. While it is true that our estimated central value of $(V - I)_0$ is based on the RC color measurements in the outer disk, beyond 3° from the LMC center, while the $(V - I)_0$ of Górski et al. (2020) is based on the central part of the LMC, the difference is nevertheless larger than expected. Because we have accounted for the metallicity, and hence color gradient, in the LMC, it is unlikely that our estimated intrinsic color in the inner parts of the LMC differs by as much as 0.045 mag.

This is further supported by a comparison of RC color measurements in this work and in Górski et al. (2020). Figure 19 presents a comparison of measured $(V - I)$ in the MCs, where panels (a) and (c) show a two-dimensional map of differences that are color coded. The histogram of differences between $(V - I)$ color values from this work and from Górski et al. (2020) is shown in panel (b) for the LMC and in panel (d) for the SMC. In the case of the LMC, the mean difference is only -0.005 ± 0.021, and in the SMC it is -0.004 ± 0.018, which shows that color estimates are consistent. Significant discrepancies in the galaxy centers are largely due to large differential reddening and disappear in panels (e) and (f), where the RC color differences are divided by the σ of the color

---

[5] Choi et al. (2018) intend to correct their map to conform with the FITS-WCS standard (Y. Choi, 2020, private communication).

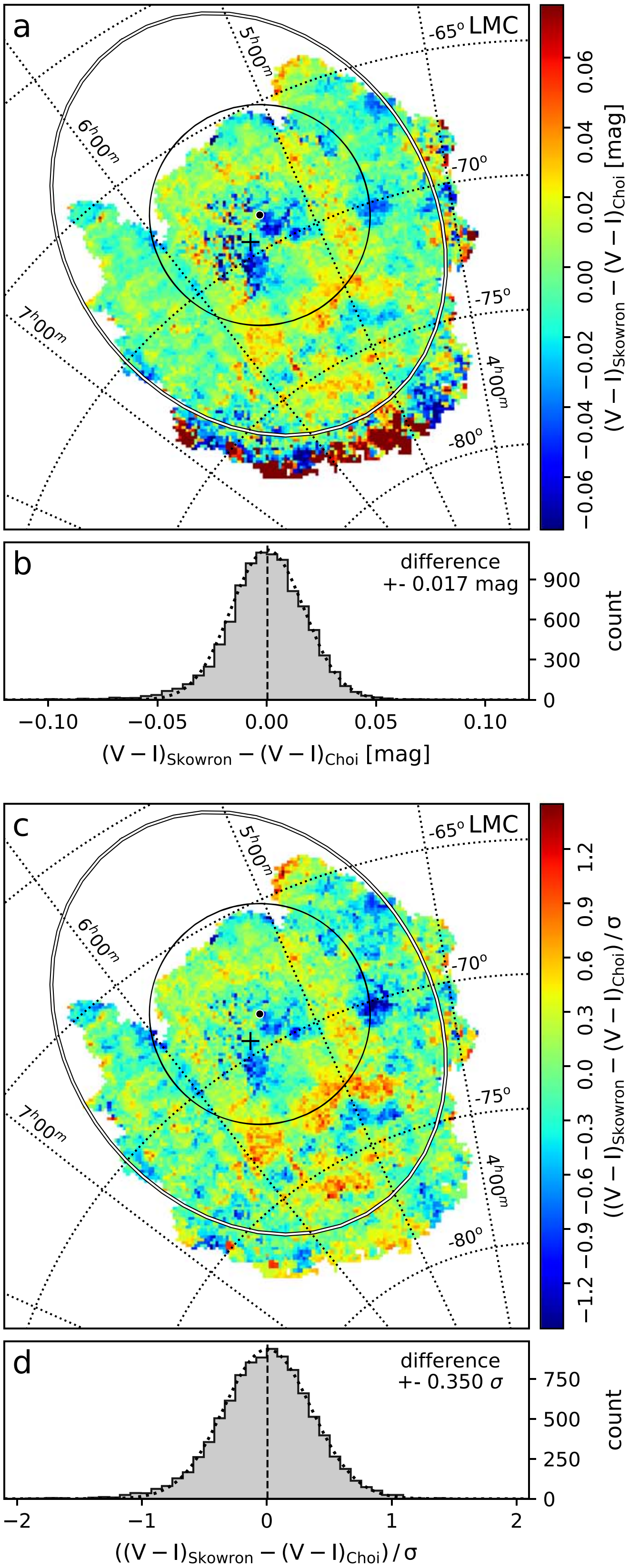

Figure 18. The comparison of color measurements from this work and the work of Choi et al. (2018) as a two-dimensional map of RC color differences (panel (a)) and as a histogram of color differences (panel (b)) in the LMC. Panel (c) shows the two-dimensional map of RC color differences divided by the σ of the color distribution, while panel (d) shows the corresponding histogram.

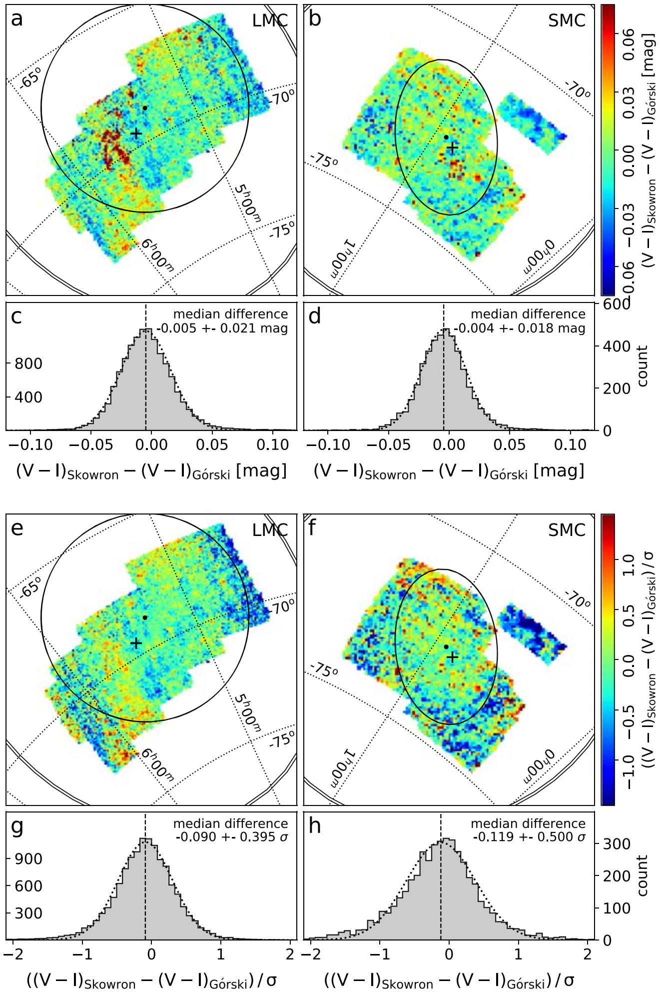

Figure 19. The comparison of color measurements from this work and the work of Górski et al. (2020) as a two-dimensional map of RC color differences in the LMC (panel (a)) and SMC (panel (c)), and as a histogram of color differences (panels (b) and (d)). Panels (e) and (f) show the two-dimensional map of RC color differences divided by the σ of the color for the LMC and SMC, respectively, while panels (g) and (h) show the corresponding histograms.

distribution. On the other hand, panels (e)–(f) highlight discrepancies in areas where the different approach to estimating the RC color plays a role.

Tables 5 and 6 in Górski et al. (2020) list separate $(V - I)_0$ values for each of the tracers used to estimate the final intrinsic color. The method using Na I line in eclipsing binaries (from Graczyk et al. 2014, 2018) has the smallest standard deviation of all four methods and gives consistent results in terms of the intrinsic color difference between LMC and SMC of 0.023 mag, which is a reasonable number and is confirmed with our data. Remaining methods tend to show smaller values of $(V - I)_0$, which can be caused either by the additional reddening or a different reddening law in the case of blue supergiants, or by systematic errors affecting reddening determinations from effective temperature for eclipsing binaries or Strömgren photometry (M. Górski, private communication). It is also worth mentioning that the standard deviation of $(V - I)_0$ obtained from the effective temperature of eclipsing binaries and atmospheric models of blue supergiants is higher compared to the standard deviation of $(V - I)_0$ obtained from

Na I line. Additionally, the intrinsic color difference between the LMC and SMC obtained from effective temperature of eclipsing binaries is zero, for blue supergiants it is only 0.01 and is as much as 0.068 mag for the Strömgren photometry, which is inconsistent with values obtained from Na I line analysis and our results. Thus, none of these values seem realistic, and combined with the high standard deviation of these methods, seem untrustworthy. Given that the method using the Na I line in eclipsing binaries gives the most reliable results, one can assume that the intrinsic color in the MCs obtained by Górski et al. (2020) should rather be 0.854 and 0.831, than 0.838 and 0.814, in the LMC and SMC, respectively. This is closer to our $(V-I)_0$ averaged within the region investigated by Górski et al. (2020), with the difference of 0.029 in the LMC and 0.031 in the SMC.

The remaining question is whether this difference between the intrinsic RC color in the outer (this work) and inner (work of Górski et al. 2020) MCs is of physical nature or is some sort of a statistical/calibration effect. The argument in favor of it being real is that we observe a dip in $E(V-I)$ in the most central part of the LMC—see Figure 15(a), where the color of the densest regions of the LMC bar is bluer than the surrounding area, which may indicate a change in the RC intrinsic color.

After verifying that our RC color measurements are consistent with those of Górski et al. (2020), we also verified our RC color measurements at the locations of eclipsing binaries from Graczyk et al. (2014, 2018) and found very similar values as Górski et al. (2020), thus ultimately concluding that this is not a matter of some calibration error between OGLE-III and OGLE-IV data or significant differences in methods of RC color determination.

We then compared our $E(V-I)$ reddening values (assuming an intrinsic color gradient as determined in Sections 4.2 and 4.3) at the locations of eclipsing binaries with $E(B-V)$ reddening values for these binaries estimated using the Na I line (Graczyk et al. 2018), as was done by Górski et al. (2020). We convert $E(B-V)$ to $E(V-I)$ with $E(V-I)=1.318\ E(B-V)$. The average difference is -0.040 both in the LMC and SMC, such that our reddening is lower than that of Graczyk et al. (2018). This is fairly consistent with the difference in the intrinsic color between Górski et al. (2020) and this work (0.045 and 0.048 for the LMC and SMC, respectively). However, we found that the reddening of eclipsing binaries in the LMC estimated by Graczyk et al. (2018) should not be averaged as it depends on the density of stars, and so does the difference between reddening from Graczyk et al. (2018) and this work. Figure 20 shows the surface density of stars in the centers of the LMC (panel (a)) and SMC (panel (c)). White dots mark the locations of eclipsing binaries from Graczyk et al. (2018). Panels (b) and (d) show the change of the $E(V-I)$ difference with the surface density of giant stars. In the case of the LMC (panel (b)), our reddening measurements are similar to those of Graczyk et al. (2018) in low-density areas but become lower with growing surface density. This can be explained in two ways: either there is a decrease of $(V-I)_0$ within the very center of the LMC bar, or there is a problem with the calibration of the equivalent width of the Na I line and the reddening.

In the latter case, the potential caveat is the use of an empirical relation between gas and dust content in our Galaxy. This relation may be different in the LMC and/or change with the gas metallicity, and thus could be the source of error, although the detailed analysis of this problem is beyond our area of expertise.

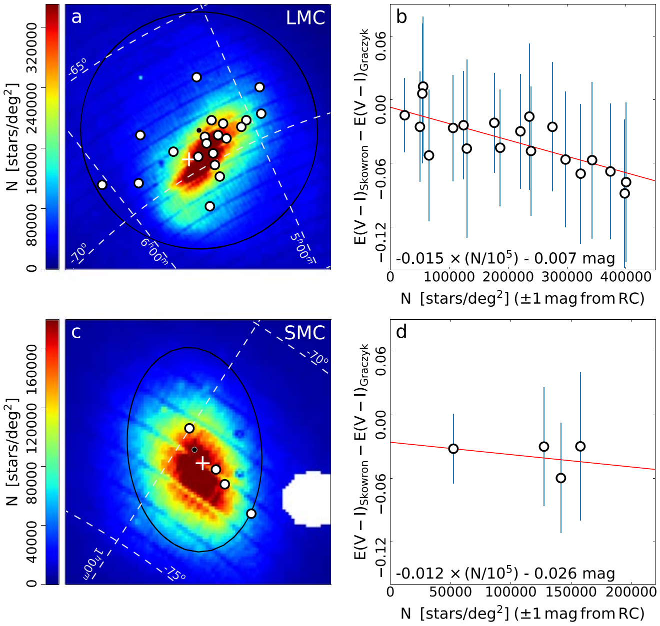

Figure 20. The distribution of eclipsing binaries from Graczyk et al. (2014, 2018) on top of the density map of stars within ±1 mag from the RC brightness in the LMC (panel (a)) and SMC (panel (c)). The $E(V-I)$ reddening difference between this work and the work of Graczyk et al. (2014, 2018), against the surface density is presented in panels (b) and (d) for the LMC and SMC, respectively.

In the former case, we have already shown that there is an increase of $(V-I)_0$ in the LMC that results from the metallicity gradient. The decrease of $(V-I)_0$ is possible for RC stars younger than 2 Gyr, which have been excluded from our analysis. However, we can compare reddening from RC stars with reddening from another tracer to see if there is a similar behavior in the bar of the LMC. If there is no dip in $E(V-I)$ in the LMC bar from another tracer, then it would mean that our $E(V-I)$ values are underestimated, i.e., the intrinsic RC color is overestimated. Figure 21 shows such a comparison between the reddening of RC stars and RR Lyrae–type variable stars. The RC sample (panel (a)) is presented in lower resolution to match the one of the RR Lyrae sample (panel (b)), where each bin contains an averaged reddening value of at least 10 stars. The RR Lyrae data were taken from Soszyński et al. (2016), the photometric metallicity values from Skowron et al. (2016) and $(V-I)_0$ was calculated with the theoretical metallicity-dependent relations from Catelan et al. (2004). It is clearly visible that the central bar area with lower reddening is also present in the reddening distribution of RR Lyrae stars. We therefore conclude that this is caused by the actual dust distribution in front of the bar region and is not a result of the change of intrinsic color.

In the case of the SMC, the $(V-I)_0$ obtained by Górski et al. (2020) is lower by 0.048 mag (or 0.031 mag if we exclude results from dubious tracers) than our intrinsic color averaged in the area investigated by Górski et al. (2020). Figures 20(c) and (d) show how the difference in reddening between Graczyk et al. (2014) and this work depends on the density of RC stars. The sample of eclipsing binaries is very small and does not span a sufficient range of stellar densities, so it is hard to draw

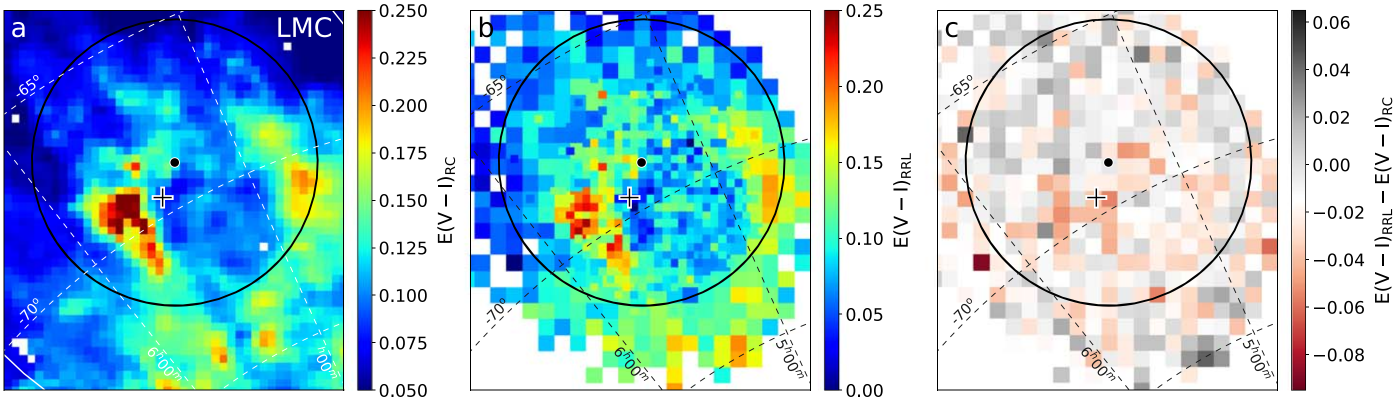

Figure 21. The comparison of $E(V-I)$ reddening from RC and RR Lyrae stars in the LMC. The reddening map of the LMC center based on RC stars is shown in panel (a). Panel (b) presents $E(V-I)$ in the same area based on RR Lyrae stars, while panel (c) shows the difference of panels (a) and (b).

explicit conclusions. With the available data, it seems that $E(V-I)$ is almost independent of the surface density of stars. This may be due to lower extinction in the SMC, lower star densities, and a small number of eclipsing binaries that could trace the potential change of their reddening with star surface density.

6. Summary

In this paper, we present the most detailed and extensive $E(V-I)$ reddening map of the MCs based on RC stars from the OGLE-IV survey (Udalski et al. 2015) that provides reddening information for 180 deg^2 in the LMC and 75 deg^2 in the SMC, with a resolution of $1\rlap{.}'7 \times 1\rlap{.}'7$ in the central parts of the MCs, decreasing to approximately $27' \times 27'$ in the outskirts. The mean reddening in the LMC is 0.100 ± 0.043 mag in the LMC and 0.047 ± 0.025 mag in the SMC.

We refine methods of calculating the RC color to obtain the highest possible accuracy of reddening maps based on RC stars. In particular, we account for the age-related additional RC structures that influence the measurement of RC color.

From the spectroscopy of red giants (Nidever et al. 2020), we find that there is a small metallicity gradient with distance from the galaxy center in both the LMC and SMC. Based on cluster data, we find a shallow dependence of intrinsic RC color on cluster metallicity. By combining the two relations, we show that there is a slight decrease of the intrinsic RC color with distance from the center. In the LMC, $(V-I)_0 = 0.886 - d \times 0.002$, where d is the distance from the galaxy center. In the SMC, $(V-I)_0 = 0.865 - d \times 0.003$ for $d > 1\rlap{.}^\circ5$, and $(V-I)_0 = 0.877 - d \times 0.009$ for $d < 1\rlap{.}^\circ5$, where d is the elliptical distance from the galaxy center. This is consistent with the results of Nataf et al. (2020), but contrary to the findings of Choi et al. (2018) and Górski et al. (2020). We also argue that the low value of $(V-I)_0$ obtained by Górski et al. (2020) is a result of using unreliable tracers, combined with possible calibration errors.

The reddening map is available from the OGLE website at http://ogle.astrouw.edu.pl/cgi-ogle/get_ms_ext.py both for download (in TEXT and FITS formats, for the users' convenience) and in the form of an interactive interface.

The presented map covers the entire area where the RC is detectable and where the spatial resolution it provides is better than that of the SFD reddening map, thus exhausting the possibility of extending the detailed reddening map of the MCs with the future RC data.

We thank Marek Górski and David Nataf for fruitful discussions on reddening in the MCs. We also thank the referee for their valuable suggestions that led to many improvements of this paper. The OGLE project has received funding from the NCN grant MAESTRO 2014/14/A/ST9/00121 to A.U. D.M.S. has received support from the NCN grant 2013/11/D/ST9/03445.

This research has made use of the NASA/IPAC Infrared Science Archive, which is operated by the Jet Propulsion Laboratory, California Institute of Technology, under contract with the National Aeronautics and Space Administration.

Funding for the Sloan Digital Sky Survey IV has been provided by the Alfred P. Sloan Foundation, the U.S. Department of Energy Office of Science, and the Participating Institutions. SDSS acknowledges support and resources from the Center for High-Performance Computing at the University of Utah. The SDSS website is www.sdss.org.

SDSS is managed by the Astrophysical Research Consortium for the Participating Institutions of the SDSS Collaboration including the Brazilian Participation Group, the Carnegie Institution for Science, Carnegie Mellon University, Center for Astrophysics | Harvard & Smithsonian (CfA), the Chilean Participation Group, the French Participation Group, Instituto de Astrofísica de Canarias, The Johns Hopkins University, Kavli Institute for the Physics and Mathematics of the Universe (IPMU)/University of Tokyo, the Korean Participation Group, Lawrence Berkeley National Laboratory, Leibniz Institut für Astrophysik Potsdam (AIP), Max-Planck-Institut für Astronomie (MPIA Heidelberg), Max-Planck-Institut für Astrophysik (MPA Garching), Max-Planck-Institut für Extraterrestrische Physik (MPE), National Astronomical Observatories of China, New Mexico State University, New York University, University of Notre Dame, Observatório Nacional/MCTI, The Ohio State University, Pennsylvania State University, Shanghai Astronomical Observatory, United Kingdom Participation Group, Universidad Nacional Autónoma de México, University of Arizona, University of Colorado Boulder, University of Oxford, University of Portsmouth, University of Utah, University of Virginia, University of Washington, University of Wisconsin, Vanderbilt University, and Yale University.

This work has made use of NASA's Astrophysics Data System Bibliographic Services.

ORCID iDs

D. M. Skowron https://orcid.org/0000-0001-9439-604X
J. Skowron https://orcid.org/0000-0002-2335-1730
A. Udalski https://orcid.org/0000-0001-5207-5619
M. K. Szymański https://orcid.org/0000-0002-0548-8995
I. Soszyński https://orcid.org/0000-0002-7777-0842
Ł. Wyrzykowski https://orcid.org/0000-0002-9658-6151
K. Ulaczyk https://orcid.org/0000-0001-6364-408X
R. Poleski https://orcid.org/0000-0002-9245-6368
S. Kozłowski https://orcid.org/0000-0003-4084-880X
P. Pietrukowicz https://orcid.org/0000-0002-2339-5899
P. Mróz https://orcid.org/0000-0001-7016-1692
K. Rybicki https://orcid.org/0000-0002-9326-9329
P. Iwanek https://orcid.org/0000-0002-6212-7221
M. Wrona https://orcid.org/0000-0002-3051-274X
M. Gromadzki https://orcid.org/0000-0002-1650-1518

References

Bell, C. P. M., Cioni, M.-R. L., Wright, A. H., et al. 2019, MNRAS, 489, 3200
Bensby, T., Feltzing, S., Gould, A., et al. 2017, A&A, 605, 89
Bica, E. L. D., Bonatto, C., Dutra, C. M., & Santos, J. F. C., Jr. 2008, MNRAS, 389, 678
Bica, E. L. D., Geisler, D., Dottori, H., et al. 1998, AJ, 116, 723
Blanton, M. R., Bershady, M., Abolfathi, B., et al. 2017, AJ, 154, 28
Carretta, E., & Gratton, R. G. 1997, A&AS, 121, 95
Catelan, M., Pritzl, B. J., & Smith, H. A. 2004, ApJS, 154, 633
Choi, Y., Nidever, D. L., Olsen, K., et al. 2018, ApJ, 866, 90
Choudhury, S., de Grijs, R., Rubele, S., et al. 2020, MNRAS, 497, 3746
Choudhury, S., Subramaniam, A., & Cole, A. A. 2016, MNRAS, 455, 1855
Choudhury, S., Subramaniam, A., Cole, A. A., & Sohn, Y.-J. 2018, MNRAS, 475, 4279
Cioni, M.-R. L. 2009, A&A, 506, 1137
Da Costa, G. S., & Hatzidimitriou, D. 1998, AJ, 115, 1934
de Vaucouleurs, G. 1960, ApJ, 131, 265
de Vaucouleurs, G., & Freeman, K. C. 1972, VA, 14, 163
Deb, S. 2017, arXiv:1707.03130
Dias, B., Kerber, L., Barbuy, B., Bica, E., & Ortolani, S. 2016, A&A, 591, A11
Dobbie, P. D., Cole, A. A., Subramaniam, A., & Keller, S. 2014, MNRAS, 442, 1680
Feast, M. W., Thackeray, A. D., & Wesselink, A. J. 1961, MNRAS, 122, 433
Fitzpatrick, E. L. 1999, PASP, 111, 63
García Pérez, A. E., Allende Prieto, C., Holtzman, J. A., et al. 2016, AJ, 151, 144
Girardi, L. 1999, MNRAS, 308, 818
Girardi, L. 2016, ARA&A, 54, 95
Girardi, L., & Salaris, M. 2001, MNRAS, 323, 109
Glatt, K., Grebel, E. K., Sabbi, E., et al. 2008, AJ, 136, 1703
Górski, M., Zgirski, B., Pietrzyński, G., et al. 2020, ApJ, 889, 179
Graczyk, D., Pietrzyński, G., Thompson, I. B., et al. 2014, ApJ, 780, 59
Graczyk, D., Pietrzyński, G., Thompson, I. B., et al. 2018, ApJ, 860, 1
Greisen, E. W., & Calabretta, M. R. 2002, A&A, 395, 1061
Grocholski, A. J., Cole, A. A., Sarajedini, A., Geisler, D., & Smith, V. V. 2006, AJ, 132, 1630
Haschke, R., Grebel, E. K., & Duffau, S. 2011, AJ, 141, 158
Hatzidimitriou, D., & Hawkins, M. R. S. 1989, MNRAS, 241, 667
Inno, L., Bono, G., Matsunaga, N., et al. 2016, ApJ, 832, 176
Jacyszyn-Dobrzeniecka, A. M., Skowron, D. M., Mróz, P., et al. 2016, AcA, 66, 149
Joshi, Y. C., & Panchal, A. 2019, A&A, 628, 51
Majewski, S. R., Schiavon, R. P., Frinchaboy, P. M., et al. 2017, AJ, 154, 94
Munari, U., & Zwitter, T. 1997, A&A, 318, 269
Nataf, D. M., Cassisi, S., Casagrande, L., & Riess, A. G. 2020, arXiv:2006.03603
Nidever, D. L., Hasselquist, S., Hayes, C. R., et al. 2020, ApJ, 895, 88
Nidever, D. L., Monachesi, A., Bell, E. F., et al. 2013, ApJ, 779, 145
Nidever, D. L., Olsen, K., Walker, A. R., et al. 2017, AJ, 154, 199
Paczyński, B., & Stanek, K. Z. 1998, ApJ, 494, 219
Parisi, M. C., Geisler, D., Carraro, G., et al. 2016, AJ, 152, 58
Parisi, M. C., Grocholski, A. J., Geisler, D., Sarajedini, A., & Clariá, J. J. 2009, AJ, 138, 517
Pejcha, O., & Stanek, K. Z. 2009, ApJ, 704, 1730
Piatti, A. E., Sarajedini, A., Geisler, D., Clark, D., & Seguel, J. 2007, MNRAS, 377, 300
Pieres, A., Santiago, B., Balbinot, E., et al. 2016, MNRAS, 461, 519
Schlafly, E. F., & Finkbeiner, D. P. 2011, ApJ, 737, 103
Schlegel, D. J., Finkbeiner, D. P., & Davis, M. 1998, ApJ, 500, 525
Sitek, M., Szymański, M. K., Skowron, D. M., et al. 2016, AcA, 66, 255
Sitek, M., Szymański, M. K., Udalski, A., et al. 2017, AcA, 67, 363
Skowron, D. M., Jacyszyn, A. M., Udalski, A., et al. 2014, ApJ, 795, 108
Skowron, D. M., Soszyński, I., Udalski, A., et al. 2016, AcA, 66, 269
Snyder, J. P. 1993, Flattening the Earth: Two Thousand Years of Map Projections (Chicago, IL: Univ. Chicago Press), 130
Soszyński, I., Udalski, A., Szymański, M. K., et al. 2016, AcA, 66, 131
Subramaniam, A. 2005, A&A, 430, 421
Subramanian, S., & Subramaniam, A. 2009, A&A, 496, 399
Subramanian, S., & Subramaniam, A. 2013, A&A, 552, 144
Tatton, B. L., van Loon, J. Th., Cioni, M.-R., et al. 2013, A&A, 554, 33
Udalski, A., Soszyński, I., Szymański, M. K., et al. 1999a, AcA, 49, 223
Udalski, A., Soszyński, I., Szymański, M. K., et al. 1999b, AcA, 49, 437
Udalski, A., Soszyński, I., Szymański, M. K., et al. 2008a, AcA, 58, 89
Udalski, A., Soszyński, I., Szymański, M. K., et al. 2008b, AcA, 58, 329
Udalski, A., Szymański, M. K., & Szymański, G. 2015, AcA, 65, 1
van der Marel, R. P. 2001, AJ, 122, 1827
Zaritsky, D., Harris, J., Thompson, I. B., & Grebel, E. K. 2004, AJ, 128, 1606
Zaritsky, D., Harris, J., Thompson, I. B., Grebel, E. K., & Massey, P. 2002, AJ, 123, 855